CrossMark

ORIGINAL ARTICLE

Experimental investigation of blast mitigation and particle–blast interaction during the explosive dispersal of particles and liquids

Q. Pontalier[1] · J. Loiseau[2] · S. Goroshin[1] · D. L. Frost[1]

Abstract The attenuation of a blast wave from a high-explosive charge surrounded by a layer of inert material is investigated experimentally in a spherical geometry for a wide range of materials. The blast wave pressure is inferred from extracting the blast wave velocity with high-speed video as well as direct measurements with pressure transducers. The mitigant consists of either a packed bed of particles, a particle bed saturated with water, or a homogeneous liquid. The reduction in peak blast wave overpressure is primarily dependent on the mitigant to explosive mass ratio, M/C, with the mitigant material properties playing a secondary role. Relative peak pressure mitigation reduces with distance and for low values of M/C (< 10) can return to unmitigated pressure levels in the mid-to-far field. Solid particles are more effective at mitigating the blast overpressure than liquids, particularly in the near field and at low values of M/C, suggesting that the energy dissipation during compaction, deformation, and fracture of the powders plays an important role. The difference in scaled arrival time of the blast and material fronts increases with M/C and scaled distance, with solid particles giving the largest separation between the blast wave and cloud of particles. Surrounding a high-explosive charge with a layer of particles reduces the positive-phase blast impulse, whereas a liquid layer has no influence on the impulse in the far field. Taking the total impulse due to the blast wave and material impact into account implies that the damage to a nearby structure may actually be augmented for a range of distances. These results should be taken into consideration in the design of explosive mitigant systems.

Keywords Blast wave mitigation · Powder compaction · Particle–blast interaction · Explosive particle dispersal

Communicated by C. Needham.

✉ D. L. Frost
david.frost@mcgill.ca

Q. Pontalier
quentin.pontalier@mail.mcgill.ca

1 McGill University, Macdonald Engineering Building, 817 Sherbrooke Street West, Montreal, QC H3A 0C3, Canada

2 Chemistry and Chemical Engineering Department, Royal Military College, 17 General Crerar Crescent, Kingston, ON K7K 7B4, Canada

1 Introduction

Blast waves generated by the detonation of high explosives are a serious hazard for nearby personnel and structures, and hence the mitigation of blast waves is an important practical concern. One common technique for reducing the strength of a free-field air blast is to surround a high-explosive charge with a layer of liquid, granular material, and/or porous cellular material. A variety of blast energy dissipation mechanisms have been proposed, and the relative importance of the different mechanisms for blast wave mitigation depends on the particular media used.

The use of a liquid layer for blast attenuation has been investigated experimentally and numerically. Numerical predictions of blast mitigation with water surrounding a spherical charge indicate that a reduction in peak overpressure by up to 80% is possible with a mass of mitigant to explosive ratio M/C of 10, although the droplet–blast interaction was not considered in this study [1]. Experimental studies using water and glycerin in a bulk form have confirmed the possibility of such a reduction [2,3], with similar mitigation

🖄 Springer

observed for the two liquids, ranging from almost 90% in the mid-field to 80% in the far field for $M/C = 34$ (water)–44 (glycerin) [3]. The blast wave attenuation implies an energy loss to the mitigant layer, which has been attributed to the acceleration of the liquid and subsequent fragmentation of the liquid into fine droplets as well as thermal effects related to liquid vaporization [1,3]. Several studies have investigated the mitigation performance using a two-phase medium such as a liquid droplet mist [3,4] or aqueous foam [5–9] within a confined area. For mists, the maximum peak blast overpressure attenuation was numerically predicted to be 70% in the mid-field, with droplet sizes of $27.5\,\mu$m and a mass loading of 2, defined as the ratio of water to gas mass within a computational cell [4]. For aqueous foams, reductions in the peak overpressure, relative to that of a bare high-explosive charge, were observed experimentally between 90 and 95%, at scaled distances between 1 and 3 m/kg$^{1/3}$, respectively [5]. The attenuation is attributed to the momentum loss in the complex 3D multiphase structure of these media and is related to the number of gas cells found within the foams [8]. The high heat capacity of the liquid phase and the compressibility of the gas bubbles also play a significant role in the mitigation process [10].

The mitigation performance of granular materials has likewise been investigated extensively. Sand has been proposed as a potential candidate [8,11] to mitigate a blast wave. In small-scale experiments, the attenuation of the peak overpressure has been observed to decrease with distance from a value of 40% in the near field to 5% in the far field with M/C between 0.1 and 0.2 [8]. Glass, steel, and ceramic [12], porcelain, plastic, claydite, and polyethylene spheres [13] have also been studied. In large-scale experiments, perlite and pumice have been used to reduce the strength of the blast wave. For example, small pockets of pumice (5.7 cm thick, $m = 1.62$ kg) placed in the far field reduced the peak blast overpressure by 66% and the blast impulse by 84% [14]. However, it is not clear, a priori, which properties of the granular media are most important for mitigation performance. Material density has been cited as a relevant parameter, suggesting that the transfer of momentum from the explosion to the particles is an important determinant of blast attenuation [2]. Porosity of the granular medium is also a significant factor, resulting in energy dissipation during the shock–medium interaction leading to compaction of the medium [2,15]. The particle size and thickness of granular layers have also been cited as potential mitigation parameters [12]. Particle crushing and rearrangement during void collapse have been proposed as other contributions to energy dissipation [14]. Compaction mechanisms have been extensively studied by research groups investigating the response of dry or water-saturated soils subjected to blast loadings [16–18]. These studies focus mainly on the shock transmission to buried structures or underground facilities and the formation of

craters [18]. Finally, the energy dissipation via acceleration of the mitigant bed has been analyzed in a companion paper as a function of the mitigant mass to charge mass M/C [19], which is correlated with the velocity of the explosively dispersed material according to classical Gurney analysis [20,21].

When a high-explosive charge surrounded by a layer of inert material is detonated, a shock wave propagates into the material, radially compacting the material to a degree which depends on the initial bed porosity, particle compressive strength, and local strength of the shock wave. When the shock wave reaches the surface of the material layer, a blast wave is transmitted into the surroundings and an expansion wave propagates back into the compacted material, causing it to expand radially outwards [22,23]. The tension induced within the compacted bed of material causes it to break up into fragments that have a size on the order of the thickness of the compacted layer when the expansion wave reaches the inner surface of the layer [24]. The fragments move radially outwards, shedding particles in their wake and leading to the formation of jet-like structures, an example of which is shown in Fig. 1. Particle jetting is a common feature of high-explosive particle dispersal; however, jet formation is not observed for particles with high compressive strength [22]. The explosive dispersal of liquids, in general, also leads to the formation of droplet jets (see Fig. 1 for an example for a layer of glycerol), although other phenomena, such as cavitation within the liquid layer behind the expansion wave, govern jet formation [25]. The explosive dispersal of liquid-saturated particle beds leads to the formation of droplet jets similar to the case of liquid dispersal and is discussed in a companion paper [26]. Although the mechanism of jet formation is not addressed in the present paper, it is of interest to determine whether or not the presence of particle/droplet jets influences the degree of blast wave attenuation.

The present study examines the relative blast wave mitigation performance of a layer of either a granular material, liquid, or a liquid-saturated particle bed surrounding a high-explosive charge in spherical geometry. A variety of different mitigant materials are tested, including powders with a range of particle size, density, and packed bed porosity, covering a
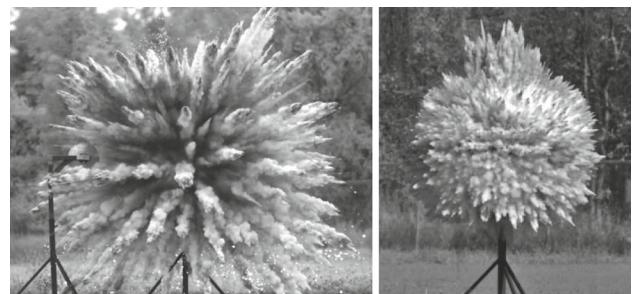

Fig. 1 Jet formation for silicon carbide powder with mass ratio M/C of 54 (left) and for glycerol with a mass ratio of 5.8 (right)

wide range of mitigant to charge mass ratios. In some experiments, the blast wave peak overpressure and impulse were obtained using fast-response pressure transducers located at various locations from the charge. The peak blast wave overpressure history very near the charges was determined with high-speed videography, by measuring the blast wave velocity with image analysis and then inferring the peak blast wave overpressure using the Rankine–Hugoniot relation. The particle–blast interaction is also investigated to quantify the potential blast pressure recovery as a function of distance. This paper is structured in the following way: Sect. 2 describes the experimental conditions, and Sect. 3 details the video processing steps used to extract the blast wave pressure. Section 4 presents the experimental results for the effect of mitigant properties on the attenuation of the blast wave pressure and impulse and a discussion of the implications of the results regarding suitable material properties for blast mitigation is presented in Sect. 5. A complimentary dataset is also attached with the paper as supplementary material.

2 Experimental overview

The charge casings used in the present study consisted of thin-walled (1-mm-thick) commercial glass light bulbs with the filaments removed. Either G40 (nominal dia 12.7 cm) or G25 (nominal dia 9.5 cm) bulbs were used. A spherical ball of C-4 (15–82 g) formed by hand was placed in the middle of the glass sphere with a plastic tube attached to allow the insertion of an electric detonator into the C-4 prior to the test. For the dispersal of liquids with a high-explosive charge, the C-4 was placed within a hollow polyethylene sphere ($m = 12.0$ g, nominal dia 3.5 cm) to isolate it from the liquid and provide a means by which the C-4 could be held rigidly in place at the center of the charge. The PE sphere was cut in half, filled with C-4, and then reassembled. The detonator tube was epoxied to the sphere and held in place with a wooden cross-piece visible at the top of the bulb in Fig. 2. Flow of detonation products up the tube perturbs the symmetry of the motion at the top of the charge (see right photograph in Fig. 1) but has no effect on the lateral motion of the material or blast. In the case of solid particles, bare C-4 charges were used. The charge was prepared by filling the sphere half full of powder, then placing the C-4 ball with attached tube in the center of the sphere, and then filling the remainder of the powder such that the C-4 was held in place by the powder. The charges were supported by a section of plastic tube attached to the end of a wooden rod, with a height of burst of 1.5 m.

For some trials, the blast overpressure was recorded with piezoelectric pressure transducers (PCB 113A24, risetime $\lesssim$ 1 μs) mounted in lollipop-style gauges (lollipop dia 30 cm) at

Fig. 2 Glass bulb with a central C-4 burster filled with either water (left) or iron powder (right). The detonator is inserted into the C-4 through the plastic tube visible protruding above the charge. The tube and C-4 are held in place by the visible wooden cross-piece which is attached to the bulb
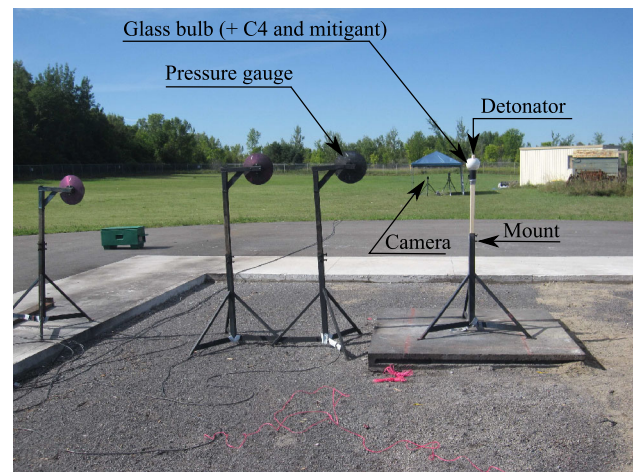

Fig. 3 Photograph of test site with charge, pressure gauge stands, and high-speed videocameras in the background

various distances from the charge (1.1, 2.0, 4.0 m), as shown in the photograph in Fig. 3. The distance for the farthest transducer was chosen such that the ground-reflected wave arrived at the transducer location after the end of the positive phase of the blast wave signature so that the positive-phase impulse measurement is not influenced by the reflected wave. It was not possible to position a gauge stand nearer than about 1 m from the charge as the direct impact of particles with the gauge obscured the blast pressure signal.

The explosive particle dispersal was recorded with a high-speed Photron SA5 videocamera recording at 10,000 fr/s. Prior to a test, a photograph of a checkerboard scale was taken to establish an absolute length scale. For a resolution of 1024×744 pixels, with a camera-charge distance of 30 m, the physical size of a pixel ranged from 3.1 to 4.5 mm, depending on the magnification. (Either a 135 or 180 mm lens was used.)

A wide variety of mitigant materials were tested. Solid particles included: Chronital S-30 stainless steel shot (Vulkan Blast Shot), SAE J827 standard S-110 steel shot, pure iron (FE-114, Atlantic Equipment Engineers), glass (Potters Ballotini impact glass beads, #10 and #13 sizes), brass (BR-102, Atlantic Equipment Engineers), titanium (TI-109, Atlantic Equipment Engineers), aluminum (H-95, Valimet Inc.), silicon carbide (30 grit), sand (commercial toy box sand), and granulated and icing sugar (commercial products). The liquids used included water, glycerol, ethanol, vegetable oil, and sodium polytungstate, a high-density liquid used for gravity separation. To increase the density of the liquids, several glycerol trials were carried out with an equal mass of tungsten carbide powder ($1\,\mu m$, Geoliquids Inc.) added. In some trials, uniform mixtures of two powders were tested, including silicon carbide powder mixed with various volume fractions of steel or glass powder. In a subset of tests, a bed of solid particles was fully saturated with water. Bulk densities of the powders were measured experimentally by determining the mass of a known volume of powder. Depending on how the powders are tapped, the bulk density can vary. In Table 1, the average between the untapped and tapped values is reported. The particle size distributions are monomodal, with the mean size provided by the manufacturers. In total, blast wave properties were extracted from 78 trials of 27 different mixtures spanning a range of mitigant to high-explosive mass ratio (M/C) from 3.8 to 297.1. A total of 44 trials were conducted with dry powders, 21 trials with neat liquids, and 13 trials with water-saturated particles. A summary of all the trials tested is attached in the supplementary material.

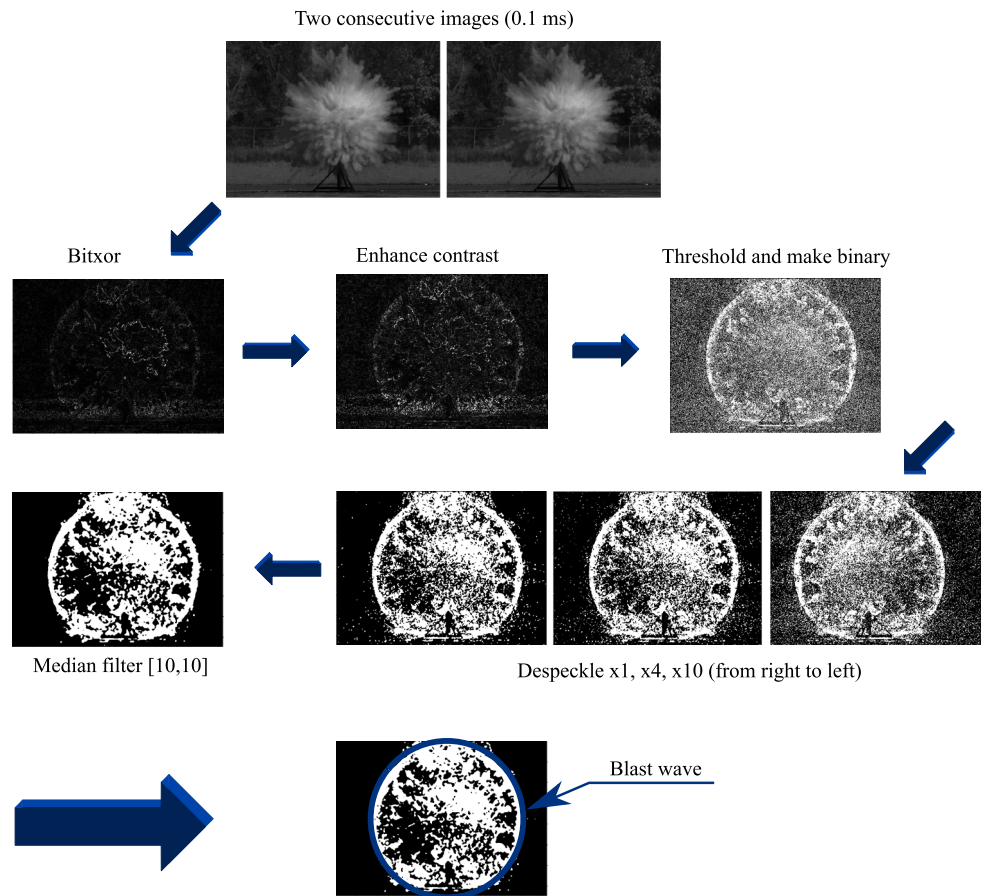**Table 1** Properties of solid particles and liquids tested

Materials	Bulk density (g/cm^3)	Mean size (μm)
Chronital steel (S-30)	4.6 ± 0.17	280
Iron (FE-114)	3.35 ± 0.34	220
Steel shot (S-110)	4.46 ± 0.33	280
Glass (Potters #13)	1.5 ± 0.08	68
Glass (Potters #10)	1.37 ± 0.16	120
Silicon carbide (30 grit)	1.67 ± 0.16	600
Aluminum (H-95)	1.50 ± 0.09	116
Titanium (TI-109)	1.78 ± 0.22	< 150
Brass (BR-102)	3.31 ± 0.45	< 150
Sand	1.67 ± 0.09	500 nom.
Granulated sugar	0.92 ± 0.07	525
Icing sugar	0.71 ± 0.16	20
Water	1	N/A
Ethanol	0.789	N/A
Glycerol	1.126	N/A
Vegetable oil	0.915	N/A
Sodium polytungstate	2.82	N/A

3 Video analysis procedure

Optical diagnostics are commonly used to visualize shock waves and blast waves. In laboratory-scale experiments, shadowgraphy, interferometry, and black-and-white or color schlieren videography are widely employed, especially in supersonic–hypersonic facilities but also for small-scale explosion tests. These techniques have been reviewed by Kleine et al. [27] and Panigrahi et al. [28]. The background oriented schlieren (BOS) [29,30] technique is largely applied to visualizing blast waves in free-field tests [31,32]. This technique consists of subtracting all the video images containing the blast front from the same, fixed image of an undistorted background. This method has also proven to be effective in visualizing underwater shock waves [33]. To improve the visualization of the blast wave in the field and diminish the errors associated with the extraction of the blast wave trajectory, it is also common to place a striped (or zebra) board behind the charge [34].

In the present paper, two different methods are used to extract the position of the spherical blast wave as a function of time and involve the use of several image processing techniques. If the blast wave peak overpressure is sufficiently high, it is possible to observe the wave front directly from the raw video images as a result of the diffraction of the background light by the density gradient across the blast wave. Once the location of the wave front has been determined, a circle may be fitted manually to the most spherical portion of the blast front. Due to a lack of symmetry of the blast wave for certain trials, the center of the circle does not necessarily correspond to the exact location of the charge but is typically very close. This procedure is repeated for each video image, maintaining the same center for all the images. If the circle does not perfectly match the wave front in all directions, the edge of the circle is placed to precisely coincide with the left side of the blast wave. The choice of the left side is motivated by the presence of pressure gauges on the right side that may slightly perturb the blast wave motion. This method has the advantage of being relatively fast (i.e., no computational time is involved), taking into account the sphericity of the blast front, and also avoiding the addition, or removal, of information associated with any image processing technique.

Above a mass ratio of around 50, the blast wave is weak enough that it is difficult to discern the blast wave front against the uneven pixel grayscale level of the background in individual video frames. To enhance the visibility of the blast front in these cases, it is necessary to perform inter-frame image processing. The choice of image processing scheme depends on the brightness, contrast, and pixel intensity of the particular trial. However, the basic procedure is to compare consecutive images so that only portions of the image that are moving (such as a blast wave) are retained. This method differs slightly from the BOS technique since the video images

Fig. 4 Different steps of video processing

Two consecutive images (0.1 ms)

Bitxor

Enhance contrast

Threshold and make binary

Median filter [10,10]

Despeckle x1, x4, x10 (from right to left)

Blast wave

are not subtracted from a unique image but rather subtracted from the previous image. At this point, various routines are used to enhance the image contrast, apply a thresholding function, filter the image, and despeckle the image until the blast wave front is distinctly visible. An overview of the typical sequence of image processing routines used is shown in Fig. 4. First, a Matlab Bit-xor transformation is applied to two consecutive frames. The Bit-xor function compares bits of the same pixel in the two different images and returns 0 if bits are equal and 1 otherwise. Pixels which have the same value (from 0 to 256) are converted to black, and others become more and less gray. Then, the contrast of the resulting image is enhanced (*imadjust* function) and a threshold is set to 4, 5, or 6 depending on the magnification ratio and the image properties. As a consequence, only pixels with a value above this threshold become visible. The next steps consist of removing the noise from the images. In the first instance, images are converted to binary, i.e., black and white. Then, several loops (about 10) of the speckle removal algorithm are used to remove the smallest noise structures. This algorithm consists of a small 2D-median filter (3×3) which replaces an input pixel at a specific location by the median value of the input pixel and its 8 neighbors. If most of the pixels surrounding the input pixel are black, the output pixel will be black, and

if not, the output pixel will be white. In the end, to eliminate the largest noise structures, a larger median filter (10×10) is applied. The size of this filter depends also on the image properties. The ultimate goal of removing the undesirable pixels is to automatically fit circles to the blast wave front. Since all of the noisy pixels surrounding the blast front have been removed, it is then possible to detect the first and last white pixels on different specific lines that should belong to the blast front. Then, with at least three points, a circle may be fitted. One drawback of image processing techniques is that inevitably some information is either added to or removed from the image. In particular, the blast front may not be perfectly smooth and several "holes" on the blast front may appear (Fig. 5). The appearance of these holes is primarily attributed to the non-uniformity of the background (presence of trees in Fig. 1) and makes it difficult to accurately detect the blast front. However, in the present study, the circles are fitted manually since the holes are too numerous on the processed images. Several image processing techniques may be applied to reconstruct the blast wave front by pixel interpolation. The use of a uniform background would also serve to decrease the numbers of these undesirable image artifacts. After applying the various image processing techniques, care must be taken to distinguish the front of the particle cloud,
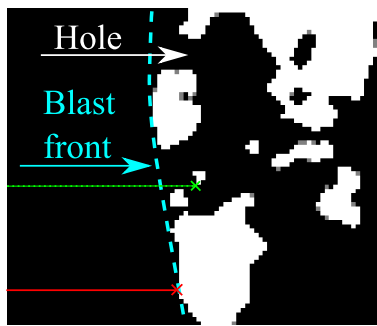
Fig. 5 Close-up of blast wave front from a processed image. Due to non-uniformities in the initial background image, "holes" may appear in the blast wave front. Under these circumstances, a circle is manually fitted to the blast wave front
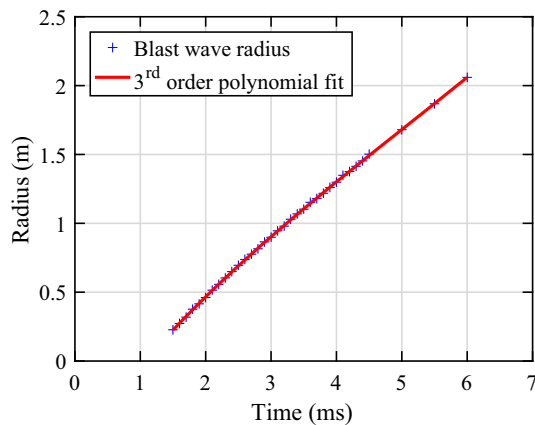

Fig. 6 Blast wave radius as a function of time for the high-explosive dispersal of titanium particles saturated with water with $M/C = 42.69$. Blue crosses refer to the blast radius extracted at a specific instant. The red line corresponds to a 3rd-order polynomial fit. To obtain the velocity profile, this fit is differentiated

which may appear as a front similar to a shock wave, from the blast wave front itself. Once the trajectory of the blast wave has been unambiguously identified, the procedure for fitting a circle to the blast wave described previously is applied.

With the image analysis procedure described above, the spherical blast radius can be determined. Pixel counts are converted to distance via the pre-trial scale image. Intra-frame positions and times are used to determine the shock trajectory, and the shock velocity is extracted by differentiating a polynomial line of best fit to the position–time data points. Figure 6 shows an example of a radius-time history plotted for a trial in which titanium particles saturated with water were explosively dispersed.

Several methods can be used to obtain the history of the blast wave velocity. First, the instantaneous velocity can be determined at a specific instant based on the change in position between two frames:

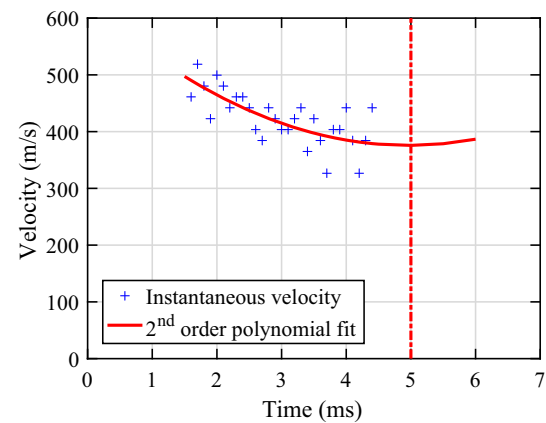$$v(i) = \frac{R(i+1) - R(i-1)}{t(i+1) - t(i-1)} \tag{1}$$

Fig. 7 Velocity profile for titanium particles saturated with water with $M/C = 42.69$. Solid red line corresponds to a 2nd-order polynomial fit (derivative of the 3rd-order polynomial fit of the position vs. time curve). Note that for the last three points of Fig. 6, instantaneous velocities are not calculable with (1), so not reported. At the right of the dotted-dashed line, data are not taken into account in the overpressure calculations

where i = image number, $R(i)$ = position of the blast in the image number i, $t(i)$ = time of the image number i, $v(i)$ = blast velocity in the image number i.

An example of the velocities calculated in this way is shown by the blue crosses in Fig. 7. The small changes in distance of the blast from one video frame to the next leads to large fluctuations in the velocity due to the lack of precision in determining the shock front location (discussed at the end of the section). To obtain a smoother variation in the blast front velocity, the shock wave trajectory is fit with a 3rd order polynomial, as shown in Fig. 6. The polynomial is then differentiated to get the velocity history, which is shown as the solid red curve in Fig. 7. This fitting function works well for trials with a mass ratio above 11. However, for mass ratios below this value, the fit is not accurate enough, especially at early times. As a result, in the range of mass ratio between 3.7 and 11, a rational mode fit, i.e., a ratio of a linear function and a second-order polynomial, as shown below in (2),

$$R(t) = \frac{at + b}{a't^2 + b't + c'} \tag{2}$$

is chosen instead. A comparison between the two fitting functions for a low value of M/C is shown in Fig. 8. Note that at later times, the velocity fitting function starts to increase and diverge from the instantaneous velocity values. This occurs due to the nature of the fitting function, which reaches a minimum and then increases. Hence, at later times, the curve fits do not follow the velocity data points, which tend to reach a plateau value. This is a non-physical behavior, and hence the velocity values to the right of the vertical dashed lines are discarded.

The Mach number and the pressure ratio across the shock are then determined from the velocity profile. The Mach num-
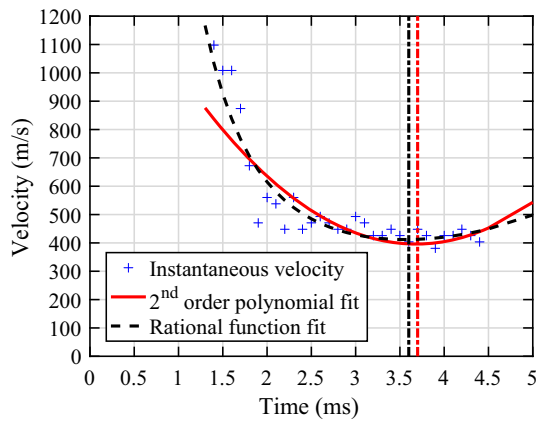
Fig. 8 Velocity profile for ethanol at $M/C = 3.76$. Solid red line corresponds to a 2nd-order polynomial fit. Dashed black line corresponds to the derivative of the rational fit of the position versus time curve. To the right of the dotted-dashed lines, the velocity begins to increase and is not considered reliable
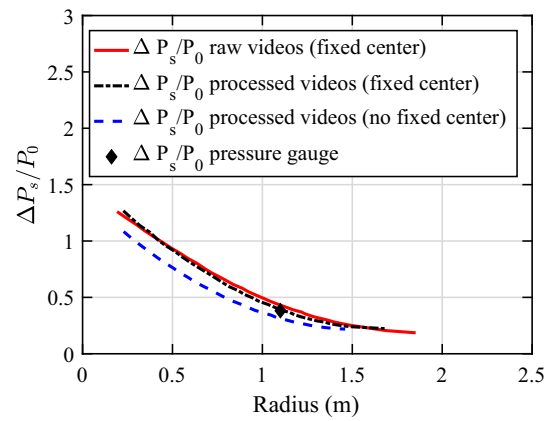

Fig. 9 Blast peak overpressure as a function of the blast radius for titanium saturated with water at $M/C = 42.69$. The red line corresponds to the overpressure extracted from raw videos. Black dotted-dashed line corresponds to the overpressure extracted from the processed video considering the center of the circle fixed and the blue dashed line considering the center not fixed. The diamond symbol indicates the value measured with the pressure transducer

ber M_a is calculated assuming the air acts as an ideal gas, with the speed of sound, c, given by (3), with γ taken to be constant and equal to 1.405, i.e.,

$$c = \sqrt{\gamma R T} \tag{3}$$

where c = speed of sound (m/s), γ = 1.405 (ratio of specific heats), R = 286.9 J/kg K (specific gas constant), T = temperature in Kelvins.

The blast wave is assumed to propagate into undisturbed air, at temperatures ranging from 5 to 25 °C, depending on the trial conditions. Once the speed of sound is determined, the pressure ratio across the blast can be determined using the Hugoniot jump relation (4) [35], assuming that the shock front is relatively thin, and γ is constant:

$$\frac{P}{P_0} = \frac{2\gamma}{\gamma + 1} M_a^2 - \frac{\gamma - 1}{\gamma + 1} \tag{4}$$

When the pressure ratio across the blast is extracted from the blast trajectory, it is of interest to compare the different methods of extraction, from raw videos or using the video analysis procedure to analyze any discrepancies. At an intermediate value of M/C, where both methods can be performed, the match is relatively accurate as shown in Fig. 9. However, if the center of the blast wave is not taken to be fixed during the processing, a more noticeable discrepancy appears. For the purpose of this study, the center of the circles remains fixed for all the videos analyzed.

To study the TNT equivalence of bare explosive charges, Dewey [36] and Kleine et al. [37] have suggested fitting the blast radius–time curve to the following form:

$$R(t_a) = A + B c t_a + C \ln(1 + c t_a) + D\sqrt{\ln(1 + c t_a)} \tag{5}$$

where R is the blast radius, c the speed of sound, t_a the time of shock arrival at a given location, and A, B, C, D are least-squares fit coefficients. B is often set equal to one to ensure that the blast velocity at later times approaches that of the speed of sound. The advantage of such a fit is its monotonicity. As a consequence, this fit is not associated with any changes in its trend after a certain time, as mentioned earlier for the third-order polynomial. However, this fit overpredicts the peak overpressure value compared to the first pressure gauge value and underpredicts the value for the second gauge. For the first gauge, the third-order polynomial is closer to the value obtained with the pressure transducer (Fig. 10). The last pressure gauge is not accessible for comparison as it is outside of the camera view. For the purpose of this study, since the interest is mainly in the near field, blast trajectories are fitted with the third-order polynomial for all the trials tested.

The number of parameters that influence the precision of the pressure measurements from pressure transducers or from high-speed videography are numerous. Some variation in the experimental parameters is inevitable, including the centering of the burster charge, the packing fraction of the powder, presence of voids within the C-4 burster charge, and so on. Pressure transducers are also subject to spurious signals from fragment impact as well as baseline drift from thermal effects. Estimation of the peak overpressure from the video extraction procedure is also subject to multiple sources of error, including errors in scaling the distances and errors in determining the shock front location from a lack of contrast or a non-uniform background. Furthermore, in the very near field, the presence of hot reacted gas (fireball) and particles projected ahead of the blast wave front may modify its prop-
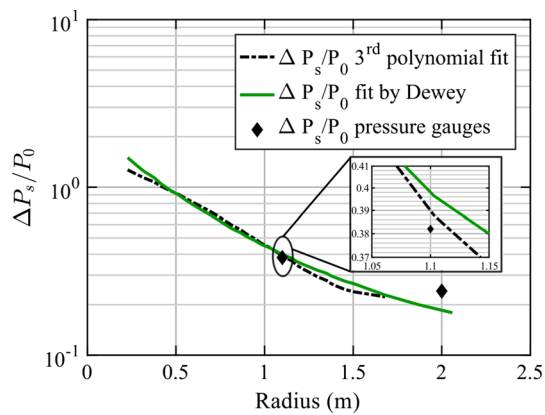
Fig. 10 Comparison of peak overpressures between the 3rd-order polynomial and the fit by Dewey and Kleine for titanium particles saturated with water at $M/C = 42.69$ from processed videos (the centers of the circles are fixed). At 1.1 m, the peak overpressure value for the third-order polynomial is closer to the value obtained with the pressure gauge as compared to the other fit. The fit by Dewey and Kleine enables to access a more extensive range but underpredicts the pressure gauge measurement at 2.0 m. The camera view does not include the last gauge, and hence the comparison at 4.0 m is impossible

agation rate. Due to the higher temperature compared to the ambient air, the speed of sound c, the Mach number M_a, and value of γ will be modified and hence the assumption of a constant value of γ in (4) is no longer valid.

A rough estimation may be obtained for the error associated with the extraction of the blast front position. This error is one or two pixels, but is averaged by the fitting process of the radius-time curve, and a value of one pixel is retained. Depending on the distance from the charge and M/C, the corresponding error in velocity is estimated to range from a maximum of 40 m/s for blast fronts far from the explosion center and for high M/C, to a maximum of 100 m/s in the near field and for low M/C. In percentage, the error linked to the estimation of the velocity and the Mach number corresponds to about 10%, and will be multiplied by 2 (20%) when converted to peak pressure due to the square exponent of the Mach number in (4).

Due to the difficulty in precisely calculating the error margins for the reasons noted above, and for clarity, the error bars have been removed on all the following plots to facilitate a more direct comparison between the results. The reproducibility of the method is analyzed in the following sections and also illustrated in the supplementary material by comparing trials at similar M/C. The degree of scatter in the results for trials with the same materials with similar M/C values is illustrated by comparing curves (e) and (f) for glass from Fig. 12 (although the particle size differs in these two trials) and curves (h) and (j) for water in Fig. 17. Discrepancies between the peak pressures inferred from the high-speed videography and values measured directly by the pressure transducer located at a distance of 1.1 m from the charge cen-

ter are analyzed in Table 2. Depending on the charge mass used (28 or 75 g), the corresponding scaled distance is either $Z = 2.34$ m/kg$^{1/3}$ or $Z = 3.25$ m/kg$^{1/3}$. The comparison for dry powders is limited to two types of material, including S-110 steel shot, Ballotini impact glass beads (both #10 and #13 sizes). The errors calculated range from zero to a maximum discrepancy of 12.5%. Note that the conversion of the peak pressure into peak overpressure and the use of the logarithmic scale in Figs. 12 and 17 and the figures presented in the supplementary material exaggerate these errors.

4 Results

In this section, the experimental results are presented in the following way. Section 4.1 presents the typical blast pressure histories recorded with pressure transducers. Section 4.2 details the results relative to peak overpressures for both granular mitigants and liquids or liquid/powder mixtures. In Sect. 4.3, a comparison is made between the arrival times of blast waves with that of particles. Finally, in Sect. 4.4, a comparison of positive-phase impulses is given for both types of material.

4.1 Blast overpressure profile

In addition to the estimation of peak blast overpressure using image analysis of the blast wave trajectories, overpressure measurements were obtained with piezoelectric pressure transducers in selected trials. (All the values are reported in the supplementary material.) The pressure gauge data were limited to measurements at either three or five specific locations and were placed relatively far from the charge so that the pressure field very near the charge was not obtained. In the near field, the glancing impact of high-velocity particles with the transducer can introduce spurious spikes on the pressure signals. Pressure gauges were triggered as soon as the blast passed the first gauge. Figure 11 illustrates the typical overpressure measurements obtained with the gauges at three different locations for the dispersal of glass particles saturated with water, with $M/C = 62.3$, recorded with a time resolution of 0.2 or 5 μs. (Oscilloscope time resolution for each trial is reported in the supplementary material.) For aesthetics, the high-frequency noise in the signals due to impact of the particles with the gauge or gauge stand has been smoothed with a Savitzki–Golay filter with a first-order polynomial and a frame size of 21, on the curves of Fig. 11. Nevertheless, the peak blast overpressures have been determined using the raw pressure data. As any spurious high-frequency noise fluctuations make a negligible contribution to the blast impulse, the blast impulses have been calculated using the trapezoid method of integration using the raw data. Note that for each curve, the second pressure

Table 2 Comparison between peak pressures obtained with the video analysis and pressure gauge measurements at 1.1 m from the explosion center

| Materials	C (g)	M (g)	M/C	Scaled distance Z (m/kg$^{1/3}$)	$\frac{P}{P_0}$ (videos)	$\frac{P}{P_0}$ (pressure gauges)	Difference (%)
Steel 110	75	1600	21.3	2.34	1.52	1.36	11.8
Steel 110	75	4130	55.1	2.34	1.30	1.28	1.6
Steel 110	28	4192	149.7	3.25	1.11	1.10	0.01
Glass dry #13	75	488	6.5	2.34	1.71	1.62	5.6
Glass dry #13	28	1312	46.9	3.25	1.20	1.19	0.8
Glass dry #13	28	1294	46.2	3.25	1.12	1.10	1.8
Glass dry #10	75	1328	17.7	2.34	1.40	1.43	2.1
Glass dry #10	28	1328	47.4	3.25	1.06	1.11	4.5
Glass dry #10	28	1332	47.6	3.25	1.14	1.12	1.8
Water	28	902	32.2	3.25	1.40	1.43	2.1
Water	28	374	13.35	3.25	1.48	1.48	0.0
Glass wet #13	75	676	9.0	2.34	1.94	1.83	6.0
Glass wet #13	75	1744	23.25	2.34	1.76	1.69	4.1
Glass wet #13	28	1744	62.3	3.25	1.21	1.25	3.2
Glass wet #13	28	1788	63.9	3.25	1.27	1.23	3.3
Glass wet #10	28	1830	65.4	3.25	1.26	1.25	0.08
Glass wet #10	75	1748	23.3	2.34	1.80	1.79	0.01
Titanium wet	75	3202	42.7	2.34	1.39	1.38	0.07
Titanium wet	75	3182	42.4	2.34	1.33	1.52	12.5
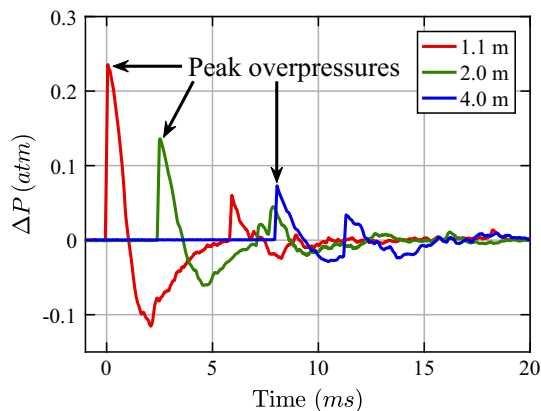
Fig. 11 Blast overpressure as a function of time captured with pressure gauges for glass (Ballotini #13 impact) beads saturated with water at $M/C = 62.3$

$$Z = \frac{R}{W^{1/3}} \tag{6}$$

where Z = scaled distance (m/kg$^{1/3}$), R = dimensional distance (m), W = (charge mass in equivalent TNT) = mass of explosive, (kg) $\times \varepsilon$ (effectiveness factor) for all tri-
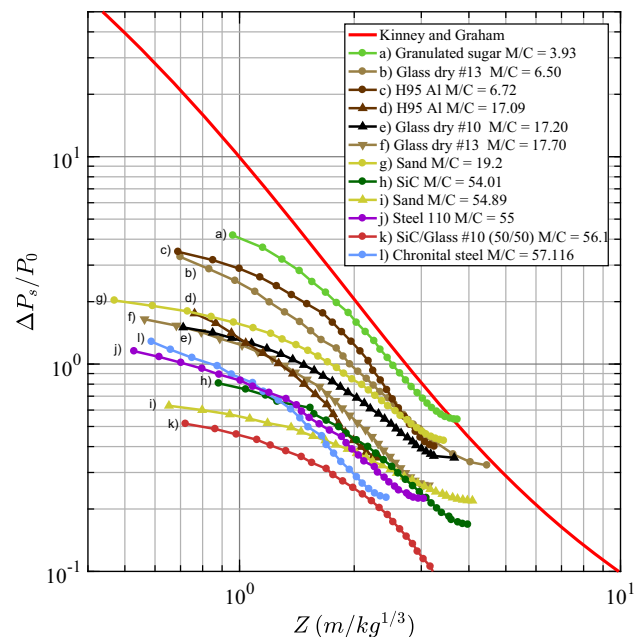

Fig. 12 Blast wave peak overpressure as a function of scaled distance, Z, for dry powders obtained by videography

spike due to the arrival of the ground-reflected wave occurs after the completion of the primary positive phase of the signal. These signals were used to determine the positive-phase impulse of the blast wave at various locations.

4.2 Peak overpressure

The peak overpressures derived from videography results are plotted as a function of scaled distance, Z, defined as,

als in subsequent sections. Following Kinney and Graham [38], the equivalent TNT charge mass, W, is equal to the mass of C-4 multiplied by an relative effectiveness factor, ε. In the present study, for peak overpressures, a value of $\varepsilon = 1.39$ is taken for C-4 which is a bit above the common value of 1.37 [39] but still in the range of accepted values (1.16–1.47 depending on the distance from the charge [40]). A value of 1.39 was chosen to fit with previous experimental data in the region of interest $0.5 \text{ m/kg}^{1/3} < Z < 12 \text{ m/kg}^{1/3}$. The normalized peak overpressure is defined by $\frac{\Delta P_s}{P_0}$, with $\Delta P_s = P_s - P_0$, with P_s representing the value of the blast peak pressure and $P_0 = 1$ atm. The scaled distance is a useful engineering parameter to compare strengths of blast waves generated by high explosives of different masses and composition. The classical blast scaling law [38] asserts that, for given atmospheric conditions, two explosions should give identical blast waves at a given scaled distance Z.

4.2.1 Granular mitigants

Figure 12 shows the peak overpressure as a function of scaled distance in a log–log plot for different dry granular mitigants and mass ratios ranging from 3.9 to 57.1. The solid red line corresponds to the peak overpressure of a bare C-4 charge based on the Kinney and Graham database [38]. This curve is based upon the assumption that the blast propagates in undisturbed atmospheric air (modeled as an ideal gas), outside of the detonation products. The peak overpressures for the eight different materials, and a mixture of silicon carbide and glass particles are shown. The curves extracted from the videos are spread over a range of scaled distances from $Z = 0.5 \text{ m/kg}^{1/3}$ to $Z = 4.0 \text{ m/kg}^{1/3}$. In some cases, the saturation of the camera sensor by the fireball radiation obscures the visibility of the blast wave front at early times. As a result, the curves do not start at the same Z values. Also, depending on M/C, the blast wave emerges from the cloud of fragments at different times and hence may be first visible at different Z values. In particular, with increasing M/C, the blast wave front is visible much closer to the charge compared to low M/C values. This phenomenon is explored more fully in Sect. 4.3.

At scaled distances less than one, the peak overpressure is reduced by about one order of magnitude with the pressure reduction increasing with increasing M/C, regardless of the mitigant material, as expected. Also, for all the materials studied, it is interesting to note that the decay rates of the mitigated overpressure curves do not follow the decay of a bare charge in air. In particular, in the near field, the blast overpressure from a mitigated charge decays significantly more slowly than for a representative bare high-explosive charge described by the Kinney and Graham curve. However, after $Z = 2 \text{ m/kg}^{1/3}$, the mitigated overpressure decay rate of certain materials approaches the decay rate of the baseline
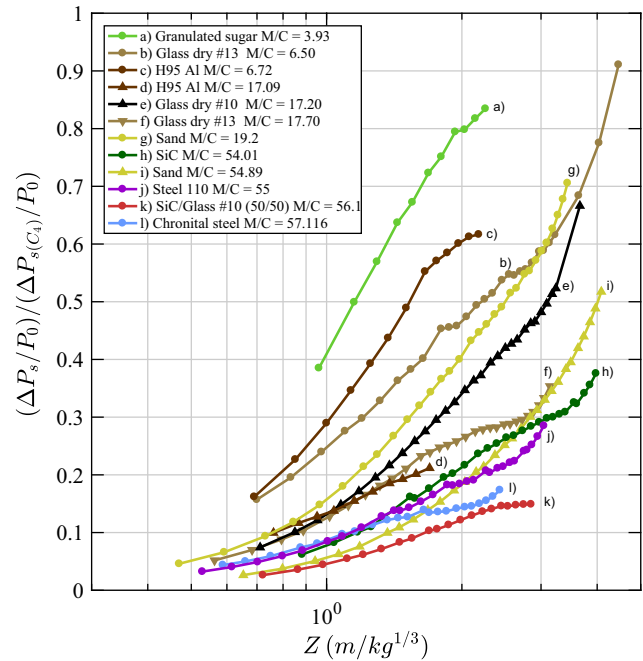

Fig. 13 Ratio of the mitigated blast wave peak overpressure over the peak overpressure of a blast wave for a bare HE charge in air (Kinney and Graham database) as a function of the scaled distance, Z, for dry powders

bare charge in air. Furthermore, for the smallest M/C value tested, the normalized overpressure recovers to almost the same value as that of an unmitigated charge in the far field.

To facilitate the comparison between the peak overpressure of the mitigated charges with a bare charge, the ratio of the mitigated overpressure to that of the baseline case for a bare charge from Kinney and Graham is shown in Fig. 13 for all reported trials with dry powders. The greatest degree of mitigation occurs at small scaled distances, and the pressure mitigation decreases monotonically with distance from the charge. For clarity, the ends of several curves have been omitted (not represented on the graphs), when the artefact of the velocity fitting procedure described earlier produced errors in the velocity (and hence blast pressure). However, the pressure attenuation continues to decrease in the far field as shown in Fig. 16.

Adding more material mass for a given high-explosive mass increases the mitigation effect in the near field (Fig. 13), with mitigated pressures normalized with the baseline case ranging from a low value (i.e., greatest pressure mitigation) of 2.6% at $Z = 0.7 \text{ m/kg}^{1/3}$ for a mixture of SiC and glass with $M/C = 56$, to a high value of 91% at $Z = 4.5 \text{ m/kg}^{1/3}$ for glass dry #13 with $M/C = 6.5$.

To illustrate the dependence of pressure mitigation on M/C in the near field to mid-field, two values of scaled distance were arbitrarily chosen ($Z = 0.8$ and $1.5 \text{ m/kg}^{1/3}$) and then at these values of Z, the corresponding mitigated overpressure
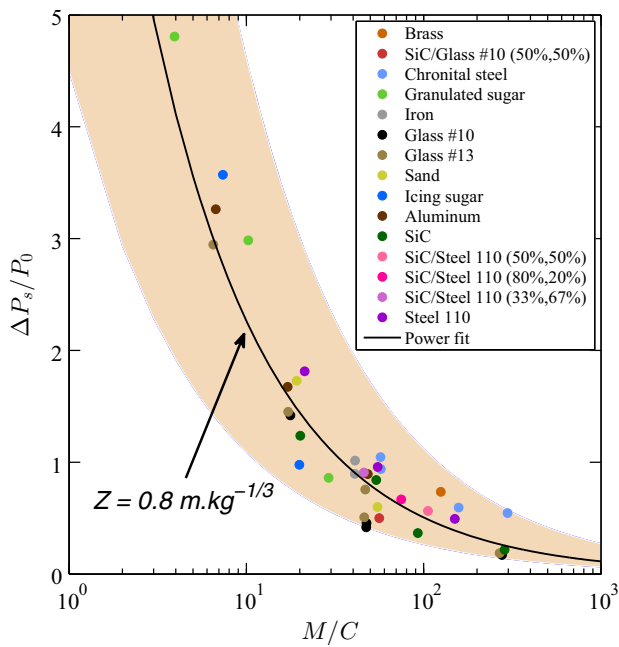
Fig. 14 Blast wave peak overpressure as a function of M/C at $Z = 0.8$ m/kg$^{1/3}$ in the case of solid powders. Data points for granulated sugar ($M/C = 3.93$) and SiC ($M/C = 54.01$) have been extrapolated from Fig. 12. The data point for brass at $M/C = 46.85$ is obscured by other data points and thus is not visible

Fig. 15 Comparison between blast wave peak overpressure of different solid powders as a function of M/C at $Z = 0.8$ m/kg$^{1/3}$

values were extracted from Fig. 12. Figure 14 shows the results for the mitigated overpressure as a function of M/C for $Z = 0.8$ m/kg$^{1/3}$ clustered within a broad band. (Data for $Z = 1.5$ m/kg$^{1/3}$ are omitted for clarity but are reported in the supplementary material.) At each scaled distance, the overpressures are reduced with increasing M/C. The decay rates are a weak function of M/C and can be represented by the following power law fits:

$$\frac{\Delta P_s}{P_0} = \alpha \times \left(\frac{M}{C}\right)^{-\beta} \tag{7}$$

where

$(\alpha, \beta) = (10.14, 0.651)$ for $Z = 0.8$ m/kg$^{1/3}$

$(\alpha, \beta) = (5.64, 0.611)$ for $Z = 1.5$ m/kg$^{1/3}$

The reproducibility of the results using the videography method can be analyzed by comparing the results for trials for a specific material at similar M/C values, e.g., Chronital steel ($M/C \approx 57$), glass #10 and #13 ($M/C \approx 47$) or iron ($M/C \approx 41$). A maximum discrepancy of 14% in terms of peak pressure is observed for glass #13. The M/C ratio appears to be the primary factor in reducing the overpressure for a given Z value, and the solid particle material properties play a secondary role. To quantify the influence of different types of materials at a specific M/C value on the overpressure reduction, each set of materials possess-
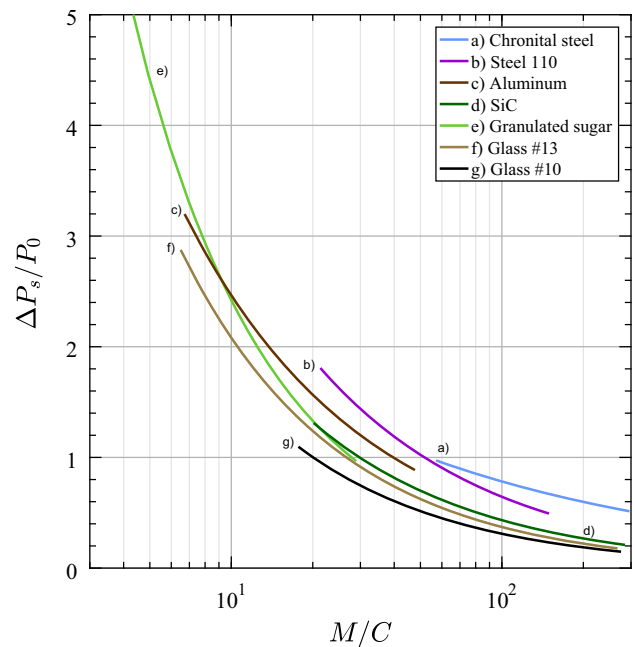
ing at least three data points has been fitted with similar power laws in Fig. 15. The results for the different materials fall within a broad band, but there seem to be some systematic differences in the mitigation performance. Care must be taken in comparing the differences, since the data from the various materials span different ranges of mass ratio M/C. With the above caution in mind, the peak overpressure mitigation efficiency of the powders can be sorted from the least efficient to the most efficient, respectively: Chronital steel $(\alpha, \beta) = (4.67, 0.388)$, S-110 steel $(\alpha, \beta) = (13.96, 0.668)$, H-95 aluminum $(\alpha, \beta) = (11.14, 0.655)$, SiC (30 grit) $(\alpha, \beta) = (10.48, 0.692)$, granulated sugar $(\alpha, \beta) = (17.71, 0.864)$, glass #13 $(\alpha, \beta) = (11.68, 0.749)$, and glass #10 $(\alpha, \beta) = (8.91, 0.729)$. The coefficients of the power laws indicate that the inclusion of data at very low M/C values makes the fits steeper. However, the power laws can be still considered as weak ($\beta < 1$). A maximum discrepancy of approximately 50% is obtained between Chronital steel and glass #10 at $M/C = 60$. The discrepancy between glass #10 and glass #13 is around 15% at $M/C = 20$. Trials from Fig. 14, not shown in Fig. 15, such as icing sugar and sand, have peak overpressure values comprised between the aluminum and the glass curves. Conversely, iron and brass have peak overpressure values closer to the two curves for steel. The addition of silicon carbide to S-110 steel powders appears to slightly reduce the peak overpressure compared to pure steel powders. The comparison at $Z = 1.5$ m/kg$^{1/3}$, given in the supplementary materials, indicates that the discrepancy between glass
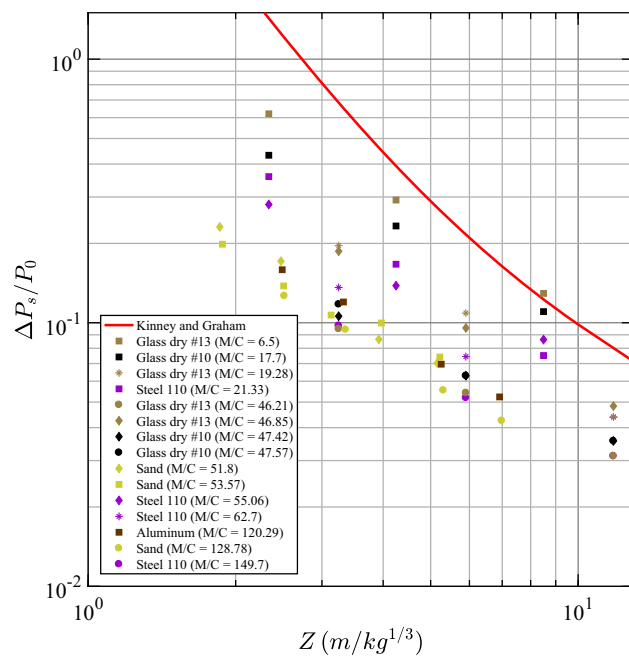
Fig. 16 Blast wave peak overpressure as a function of scaled distance, Z, for dry powders obtained from pressure gauges

Fig. 17 Blast wave peak overpressure as a function of the scaled distance, Z, in the case of liquids/powders saturated with water

#10 and Chronital steel reduces slightly to 40% but that the discrepancy between the two glass powders increases to 25%.

Peak overpressures obtained with pressure gauges in the mid-to-far field are shown in Fig. 16. As expected, the peak overpressure decreases with M/C as a weak power law and the mitigation of the peak overpressure continues to decrease with distance. The comparison between glass powders and steel indicates that glass particles continue to outperform steel at reducing the peak blast overpressure. Indeed, S-110 steel has peak overpressure values comparable to that of glass even with mass ratios about three times higher ($M/C = 149.7$ compared with $M/C \approx 47$). At $M/C \approx 20$, S-110 steel appears to have lower peak overpressure values than glass #10 but is subject to high uncertainties when comparing with the videography results (11.8%). In the same fashion, sand outperforms aluminum with comparable peak overpressure values for M/C, respectively, at 52 and 120. On the other hand, the effect of particle size for glass powders is not clear given the discrepancy (almost 50% between glass #13 at $M/C \approx 47$ and $Z = 3.24 \, \text{m/kg}^{1/3}$), but glass #13 performs better than glass #10 in the far field, contrary to the behavior in the near field at $M/C = 17$–19.

4.2.2 Liquids and powders saturated with water

In the same manner as in Fig. 12, Fig. 17 presents the decay of peak blast overpressure as a function of scaled distance for mitigants consisting of pure liquids or powders fully sat-
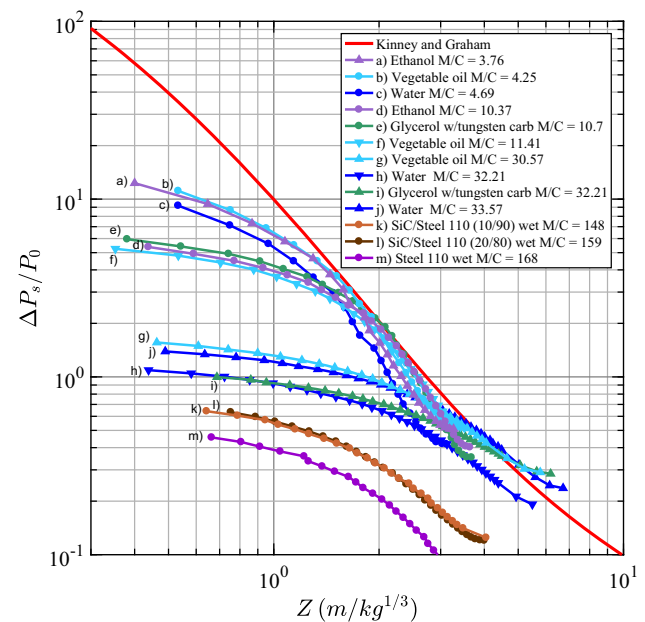
urated with water. Figure 18 presents the normalized results for the liquid and saturated particle trials. The reduction in peak overpressures with liquids and powders saturated with water surrounding the charge follows the same trend as for solid powders with large pressure reductions at small scaled distances and with the pressures approaching more closely to that of a bare charge for $Z > 2 \, \text{m/kg}^{1/3}$, except for the case of the largest values of M/C. As for solid powder, the attenuation can be quantified in the far field from the pressure gauge data (Fig. 21). From Fig. 18, the case of S-110 steel shot saturated with water, with $M/C = 168$, generates the highest attenuation with a value of 2% at a scaled distance of $Z = 0.7 \, \text{m/kg}^{1/3}$. On the other hand, for all the materials with $M/C < 35$ (except for curve h)) the peak blast overpressure recovers to a value similar to that of an unmitigated charge for scaled distances of $Z > 2 \, \text{m/kg}^{1/3}$.

A similar analysis is presented for the liquid experiments, where the peak overpressure is plotted as a function of M/C for two values of scaled distance. These results follow a similar power law decay as with the solid powders, but with different coefficients for (7): $(\alpha, \beta) = (26.37, 0.85)$ for $Z = 0.8 \, \text{m/kg}^{1/3}$ and $(\alpha, \beta) = (10.88, 0.699)$ for $Z = 1.5 \, \text{m/kg}^{1/3}$. As for solid powders, the reduction in peak overpressure for $Z = 0.8 \, \text{m/kg}^{1/3}$ as a function of M/C is shown in Fig. 19. (The graph for $Z = 1.5 \, \text{m/kg}^{1/3}$ is given in the supplementary material.) Here, the reproducibility of the videography method is given for glycerol ($M/C \approx 6$), water ($M/C \approx 30$), titanium wet ($M/C \approx 40$), and glass wet ($M/C \approx 60$). A maximum discrepancy of 13% in terms of peak pressure is observed for water.
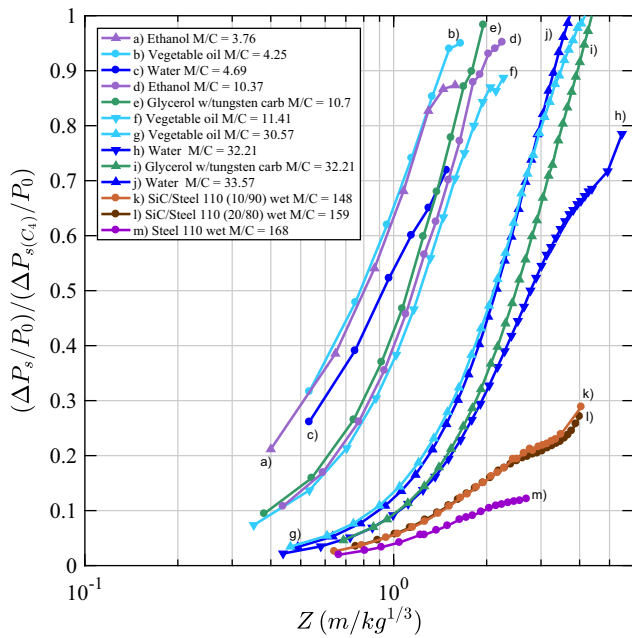
Fig. 18 Normalized blast wave peak overpressure versus scaled distance for liquids and powders saturated with water
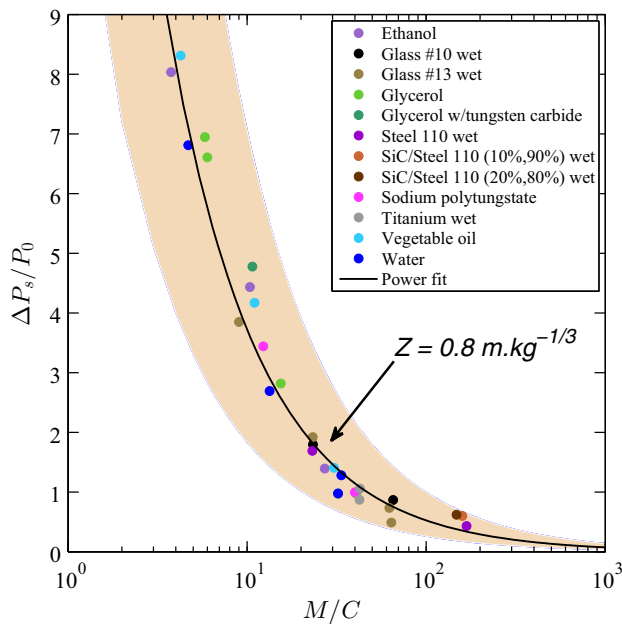

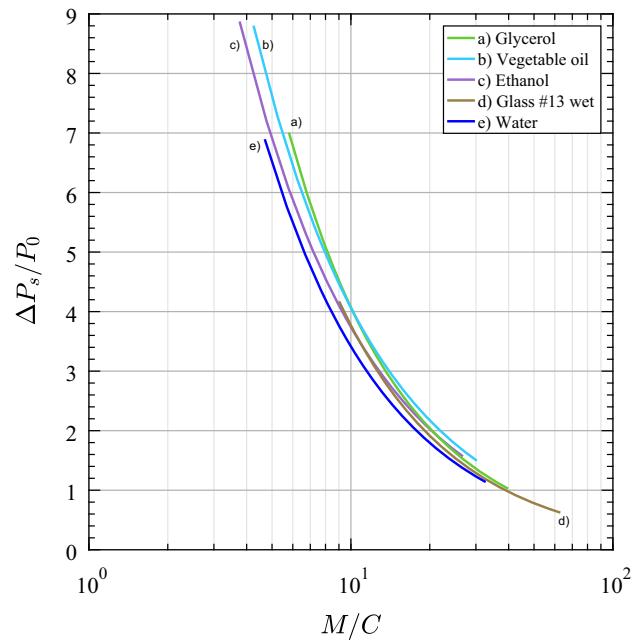**Fig. 19** Blast wave peak overpressure as a function of M/C at $Z = 0.8\,\text{m/kg}^{1/3}$ in the case of liquids/powders saturated with water. Data points for several trials are not visible because they are obscured by other data points (e.g., glycerol w/tungsten $M/C = 32.21$ is behind the water data point and similarly glycerol $M/C = 40.75$ is obscured by the sodium polytungstate data)

Blast mitigation performances can be compared on a per material basis in Fig. 20. In comparison with dry powders, the results for liquids and saturated particles as a function of M/C fall within a much tighter band, indicat-

Fig. 20 Comparison between blast wave peak overpressure as a function of M/C at $Z = 0.8\,\text{m/kg}^{1/3}$ in the case of liquids or powders saturated with water

ing that the material properties play a relatively minor role in this case. Nevertheless, water $(\alpha, \beta) = (28.94, 0.93)$ appears to produce the largest peak overpressure attenuation, whereas glycerol $(\alpha, \beta) = (40.42, 1.00)$ and vegetable oil $(\alpha, \beta) = (32.51, 0.90)$ produce the least. Ethanol $(\alpha, \beta) = (28.57, 0.88)$ and glass #13 wet $(\alpha, \beta) = (35.75, 0.98)$ fall in between with similar performances. The discrepancy between the best mitigant (water) and the worst mitigants (vegetable oil, glycerol) falls between 15 and 20%, depending on the mass ratio. At $Z = 0.8\,\text{m/kg}^{1/3}$, this discrepancy appears to increase slightly to 23–27%. The addition of tungsten carbide powder to glycerol slightly reduces the blast attenuation shown in Fig. 19 for low M/C, but the mixture has a similar mitigation performance with the other liquids at $M/C \approx 32$. Moreover, all the powders saturated with water have relatively similar mitigation performances. Nevertheless, contrary to solid powders, the effect of particle size is not clear. Indeed, at $M/C = 23$, glass #10 has a lower peak overpressure but a higher peak overpressure at $M/C \approx 63$ compared to glass #13. Peak overpressures values for sodium polytungstate fall between the peak overpressure values for glycerol and water.

As for Fig. 16, Fig. 21 presents the peak overpressure for liquids or powders saturated with water in the mid-to-far field obtained with pressure gauges. The peak overpressure mitigation, as for solid powders, decreases in the far field and scales as a weak power law of M/C. At similar M/C values, glass wet #13 attenuates the peak overpressure slightly better in the far field compared to glass wet #10. At low M/C values,
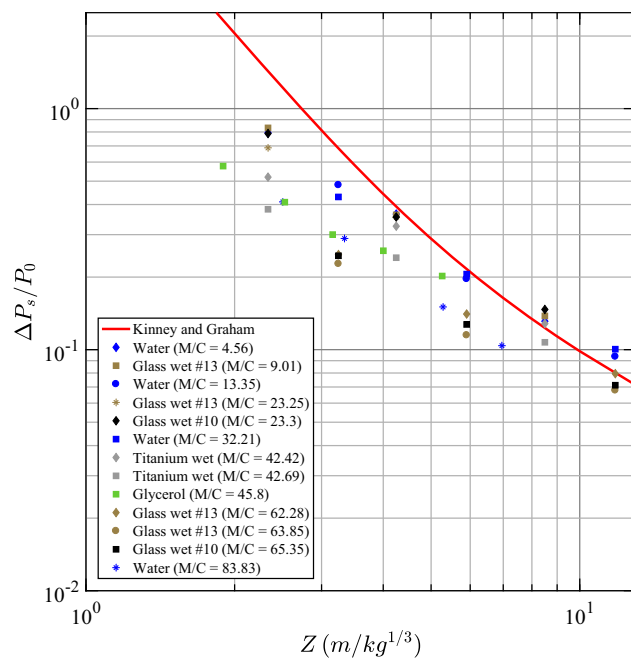
Fig. 21 Blast wave peak overpressure as a function of scaled distance, Z, for liquids or powders saturated with water obtained with pressure gauges

Fig. 22 Effective peak blast overpressure mitigation as a function of M/C for solid powders and liquids/powders saturated with water in the near field to mid-field, at two different scaled distances

water and glass wet have similar peak overpressure values, but the wetted powders have higher mitigation performances at high M/C values.

To facilitate the comparison of the peak blast overpressure attenuation performance of solid particles versus liquids (or particles saturated with water) for a given M/C ratio, the power law fits to the data shown in Figs. 14 and 19 are normalized by the value of the baseline bare charge in air and plotted in Fig. 22. In the near field, for $Z = 0.8\,\text{m/kg}^{1/3}$, for M/C values greater than about 30, the blast overpressure is highly attenuated, with values less than 10% of the value for a bare charge for both granular mitigants and liquids or water-saturated powder beds. Moreover, in the same region, for small M/C values, powders are about twice as effective at mitigating blast overpressure. As M/C increases, the differences are reduced and all materials exhibit a similar mitigation performance.

4.3 Arrival time

To visualize the relative position between the leading edge of the particles or particle jets (the method of extraction of jet trajectories is discussed in another publication [19]) and the blast wave for each trial, it is convenient to plot the arrival time of each front as a function of distance, determined from video footage, on the same graph, in the manner of Brode [41]. Similar to the scaling of distance, the arrival time may
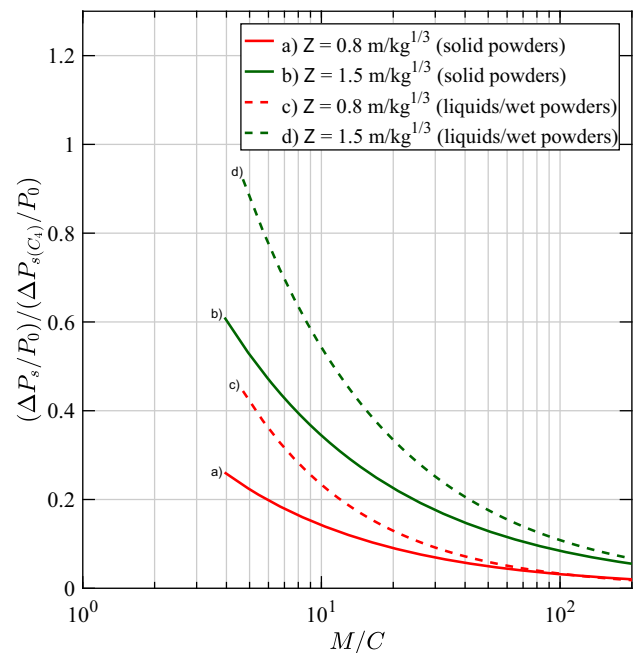
be scaled as follows:

$$t_s = \frac{t_a}{W^{1/3}} \tag{8}$$

where t_s = scaled blast arrival time (ms/kg$^{1/3}$), t_a = actual blast arrival time (ms), W = charge mass in equivalent TNT (defined previously).

Figure 23 shows the blast wave and material arrival times, as a function of Z, for three arbitrary materials at different M/C values for granular mitigants. Similarly, Fig. 24 shows the arrival times for liquids/powders saturated with water, determined using the same spherical fitting technique. Time zero corresponds to the time of detonation of the burster charge, and the material location is determined by finding the maximal spatial extent of the particles or particle jets at a given time. These graphs indicate that the trajectories of blast waves for a mitigated charge are retarded compared to an ideal blast wave for a bare high-explosive charge. For the relatively light aluminum particles, with a low value of M/C, the particles follow closely behind the blast wave. However, for steel particles with a large value of M/C, the jets lag behind the blast front at a considerable distance. For the case of liquids or powders saturated with water, the liquid droplets follow more closely behind the blast wave than for solid particles. For the case of glass powder saturated with water, it is difficult to distinguish between the glass particles and water droplets, although in this case the jets rapidly decelerate some distance from the charge, possibly due to breakup and vapor-
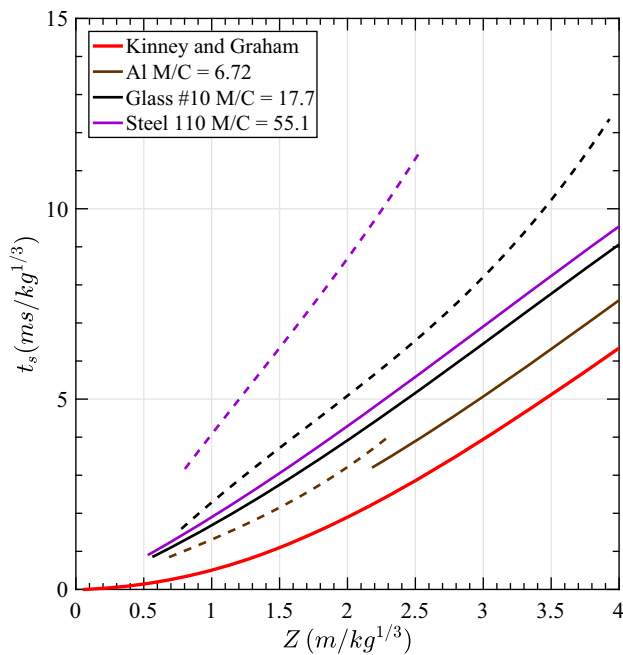
Fig. 23 Scaled time of arrival as a function of the scaled distance for granular powders. Solid lines: blast wave, dashed lines: jets
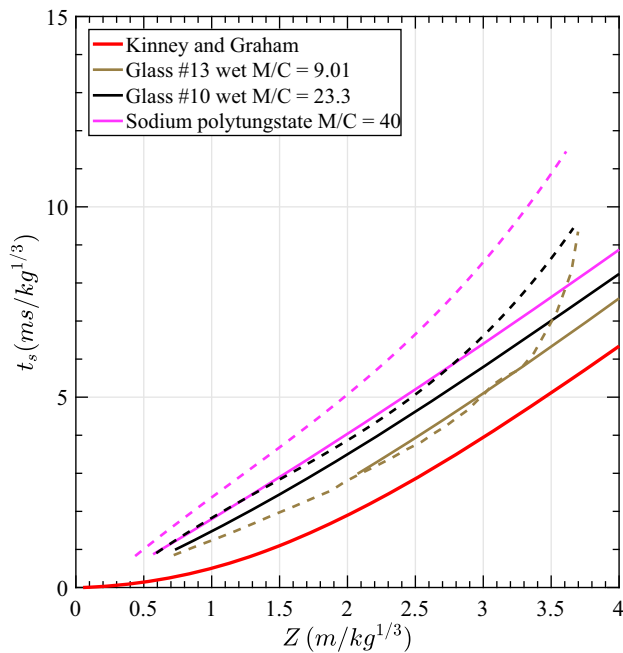

Fig. 24 Scaled time of arrival as a function of the scaled distance for liquids. Solid lines: blast wave, dashed lines: jets

Fig. 25 Single photographic frames (on the left) from three different experiments at the same scaled time (see 8) of 2.2 ms/kg$^{1/3}$ as a function of M/C. The pictures on the right show the same image, subtracted from a consecutive image, to enhance the visibility of the blast wave. No pixel noise filters are applied to the images, so scattered black pixels are still visible in the background. The top image is for the dispersal of S-110 steel shot ($M/C = 55.1$), the middle image the dispersal of dry #10 glass beads ($M/C = 17.7$), and the bottom image the dispersal of a bed of #10 glass beads saturated with water ($M/C = 23.3$). In each case the high-explosive mass is 75 g. All of the photographs are at the same scale. (The circular lollipop gauge mount, visible on the right, has a diameter of 30 cm.) Note that the jets can overtake the blast at the top of the charge due to the jetting of detonation products up the tube housing the detonator. Moreover, the jets can also penetrate the blast front on the sides in the near field and for low M/C values (see Fig. 26)

ization of the droplets. Furthermore, the jets may overtake the blast front for the lowest M/C values, as seen in Fig. 24 for $Z < 3$ m/kg$^{1/3}$.

The effect of M/C on the separation between the blast wave and the leading edge of the particle cloud is illustrated in Fig. 25, which shows a single photographic frame from
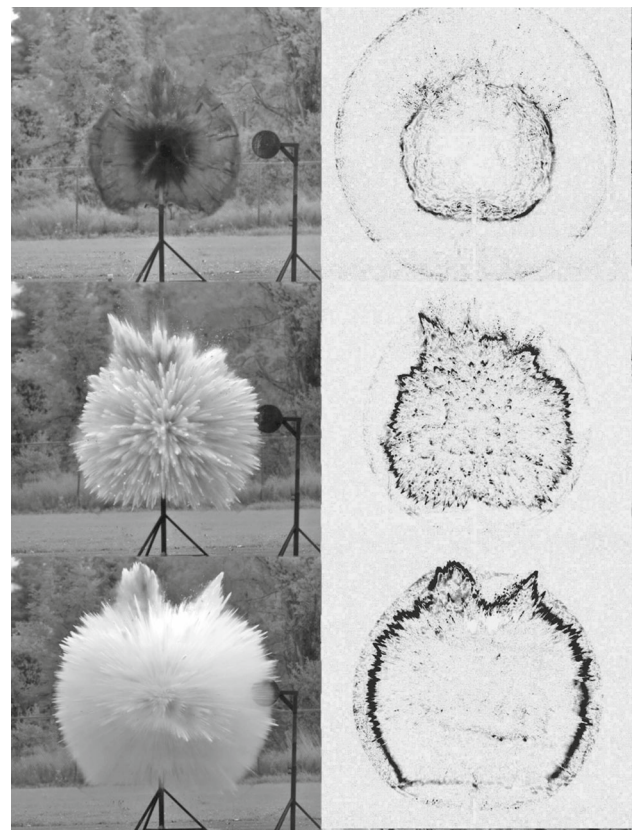
three different experiments, taken at the same scaled time of 2.2 ms/kg$^{1/3}$. For each experiment, the original photograph is shown on the left and a processed image is shown on the right. The original image is subtracted from a consecutive image to highlight the parts of the image that are moving, including the blast wave and particle fronts, such that the distance between the blast wave and particle front is readily visible. Contrary to the previous video processing technique, no pixel noise filter was applied, and hence scattered black pixels are still evident in the background. The upper two photographs show the dispersal of dry powders (S-110 steel at the top, with $M/C = 55.1$ and #10 glass powders in the middle, with $M/C = 17.7$). As the mass ratio decreases, the distance between the particle front and the blast wave
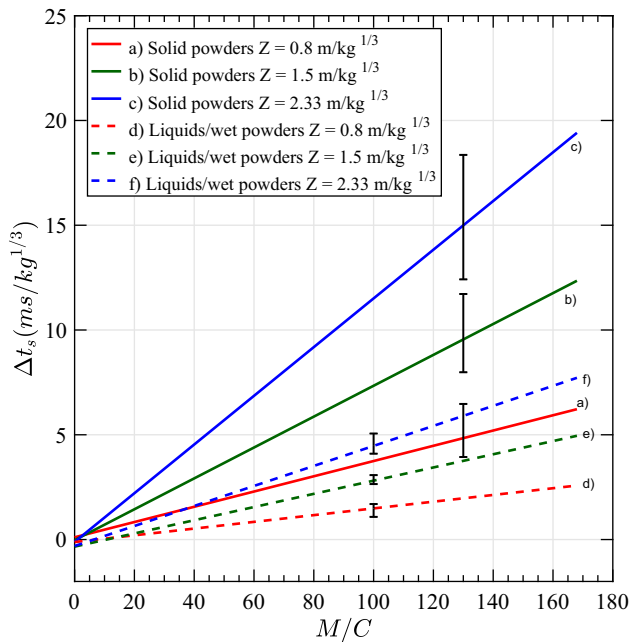
Fig. 26 Separation between blast waves and jets (difference in scaled arrival time) as a function of M/C for solid powders and liquids/powders saturated with water at $Z = 0.8\,\text{m/kg}^{1/3}$, $Z = 1.5\,\text{m/kg}^{1/3}$ and $Z = 2.33\,\text{m/kg}^{1/3}$. The negative separation for the lowest M/C values shows the possibility that the jets to overtake the blast front

decreases, as expected. The picture on the bottom shows the dispersal of a wetted bed of #10 glass powder. Even though the M/C value (23.3) is higher than for the dry powder, the material jets (a mixture of liquid and powder) for the slurry case follow more closely behind the blast wave than for the dry powder. This indicates that with dry powder beds, there is greater energy dissipation during particle dispersal and the material velocity is less.

To make a more quantitative comparison of the distance between the material front and the blast wave for liquid and granular mitigants, it is convenient to plot the difference of the scaled arrival time between the materials and the blast wave as a function of M/C in Fig. 26 according to:

$$\Delta t_s = t_{s_{\text{jets}}} - t_{s_{\text{blast}}} \tag{9}$$

To obtain such a plot, the scaled arrival times of both the blast wave and material front have been extracted from the fitted time versus distance trajectory plots. At each Z value, the difference between the scaled times was extracted for 31 trials for granular mitigants and 24 trials for liquids/powders saturated with water. For clarity, all the data points are not represented on the graph. For each scaled distance, a linear function was fitted to the data points, with the error bars representing the maximum data point divergence for the whole curves. Solid powders show the largest scatter in the results due to the difficulty in extracting an unambiguous value for

the particle front, particularly far from the charge center when the particle density is low and for non-jetting powders (e.g., steel). In the case of liquids or powders saturated with water, the scatter is mainly attributed to the differences between liquids and powders saturated with water, the latter sustaining the coherence of the jets close to the blast front over longer distances and less subject to drag.

It is clear that the difference in scaled time between the material and blast fronts increases with M/C and Z. Moreover, at given M/C and Z values, solid powders lead to the highest separation between the blast wave and the cloud of fragments. This discrepancy between liquids and solid powders continues to increase with increasing Z and M/C. Even if jets particles/droplets can overtake the blast on top of the charge due to burster/jetting effects (see Fig. 25), generally jets lag behind the blast front on the sides. However, for very low M/C values, jets may cross the blast front on the sides. This effect is indicated in Fig. 26 by the negative Δt_s values.

4.4 Positive-phase impulse

The positive-phase blast impulse is an important parameter when assessing the potential for structural damage due to blast waves. The positive-phase impulse I^+ is defined as the area under the curve of the first positive section of the overpressure curve, i.e.,

$$I^+ = \int_{t_a}^{t_f} \frac{\Delta P}{P_0}\,dt \tag{10}$$

with $t_f = t_a + t_d$, t_a being the time of arrival of the blast wave, and t_d being the duration time of positive overpressure. For the convenience of comparing results from experiments with different high-explosive masses, it is of interest to define a scaled impulse as follows:

$$I_s^+ = \frac{I^+}{W^{1/3}} \tag{11}$$

where I^+ = positive-phase blast wave impulse (bar · ms), I_s^+ = scaled positive-phase blast wave impulse (bar · ms/kg$^{1/3}$), W = charge mass in equivalent TNT (defined previously) with a relative effectiveness factor $\varepsilon = 1.15$ in the definition of W, which was determined empirically by Bogosian et al. [40], and differs from the relative effectiveness factor for pressure. The impulse data are obtained for all trials by integrating the blast overpressure-time history obtained with the side-on piezoelectric pressure transducers. The trapezian method of integration has been used with a minimum of 140 points associated with the positive overpressure phase. The time resolution of the pressure measurements was between 0.2 and 5 μs (depending on the trial—see supplementary material). Another method for determining blast
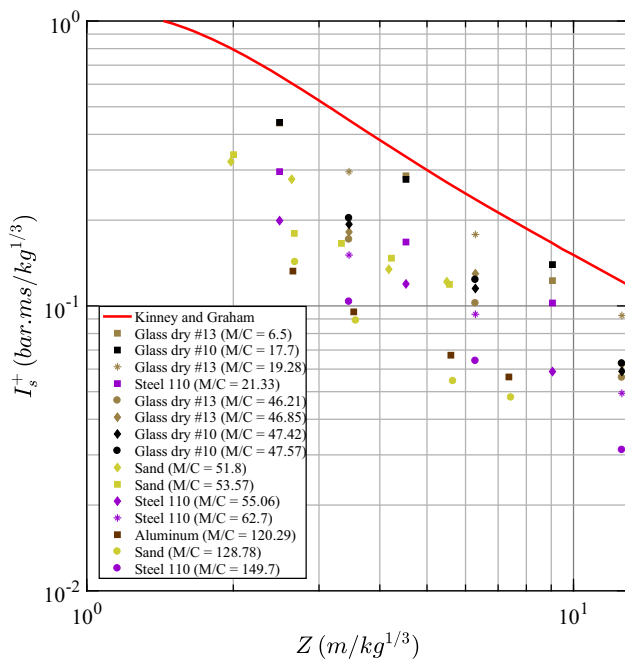
Fig. 27 Scaled positive-phase blast wave impulse as a function of scaled distance Z for the case of solid powders

Fig. 28 Scaled impulse as a function of M/C at three different scaled distances Z for solid powders. Green-edged dots are extrapolated from Fig. 27

impulse using optical data to characterize the density gradients within the flow field has been reviewed by Biss and McNesby [42]. This method is not practical in the present situation due to the presence of a non-uniform background and the presence of compacted fragments that perturb the local pixel intensity. In this data set, due to the high density of particles in the near field, pressure gauges are located relatively far from the charge center corresponding to a scaled distance between $Z = 1.98$ m/kg$^{1/3}$ to $Z = 12.57$ m/kg$^{1/3}$.

4.4.1 Impulses for dry powder mitigants

Figure 27 presents the scaled impulse results for five different types of powders. In all cases, the blast impulse falls below the values for a bare charge from Kinney and Graham, by up to a factor of 5. The spread in the results is the result of variations in the M/C value. Reproducibility of the results can be obtained by comparing glass #10 and #13 at $M/C \approx 47$. The maximum discrepancy is found to be 21% for glass #13 at $Z = 6.29$ m/kg$^{1/3}$.

At high M/C values, aluminum and sand have lower impulse values compared to steel even if their mass ratios are lower (120.29 and 128.78, respectively, compared to 149.7) suggesting that steel particles attenuate less. However, at an M/C value around 50, the impulses between sand and steel are relatively similar for Z just above 2 m/kg$^{1/3}$, but a discrepancy appears for higher Z and steel impulses are more reduced. This discrepancy is attributed to the noisy overpressure-time signal for the sand trial. Also, at $M/C =$
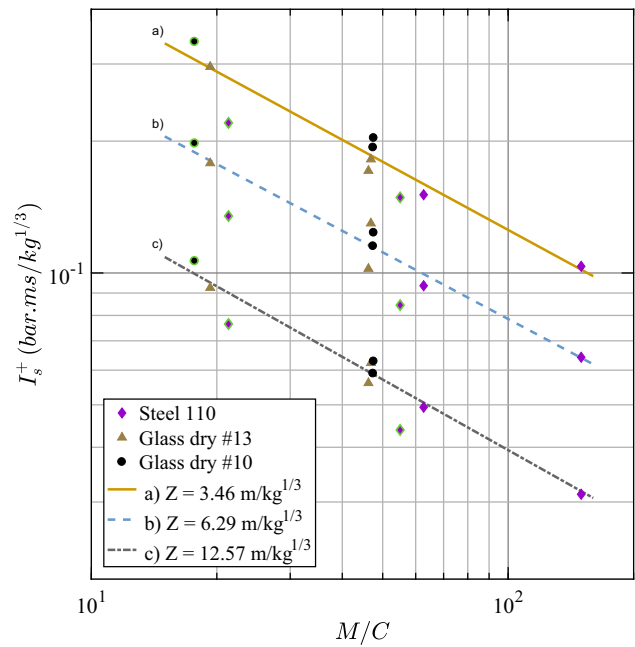
21.3, steel generates similar impulses as glass at $M/C \approx 47$. Particle size seems also to affect the impulses. Contrary to peak overpressures in the near field, glass #13 particles appear to attenuate the impulses more at $M/C \approx 47$. Also, glass #13 $M/C = 6.5$ appears to have similar impulses (or even lower for $Z > 8$ m/kg$^{1/3}$) compared to glass #10 $M/C = 17.7$. Figure 28 shows the average dependence of scaled impulses with M/C for 3 different Z values for M/C between 17.7 and 149.7. The data can be fit once again with power law fits (straight lines in logarithmic scale) according to (7) with the following coefficients:

$(\alpha, \beta) = (1.356, 0.517)$ for $Z = 3.46$ m/kg$^{1/3}$

$(\alpha, \beta) = (0.807, 0.506)$ for $Z = 6.29$ m/kg$^{1/3}$

$(\alpha, \beta) = (0.463, 0.535)$ for $Z = 12.57$ m/kg$^{1/3}$

For comparison, several data points for steel and glass #10 have been extrapolated from Fig. 27 and added to Fig. 28. Steel particles appear to have lower positive-phase impulses compared to glass, especially for $M/C < 63$. Conversely, on average, glass #13 has lower impulses compared to glass #10.

4.4.2 Impulse for liquid and water-saturated powder mitigants

In a similar manner, the scaled impulses for liquids and liquid-saturated powders are plotted as a function of Z and M/C (for given Z values) in Figs. 29 and 30, respectively. In the far field, most of the positive-phase impulses are
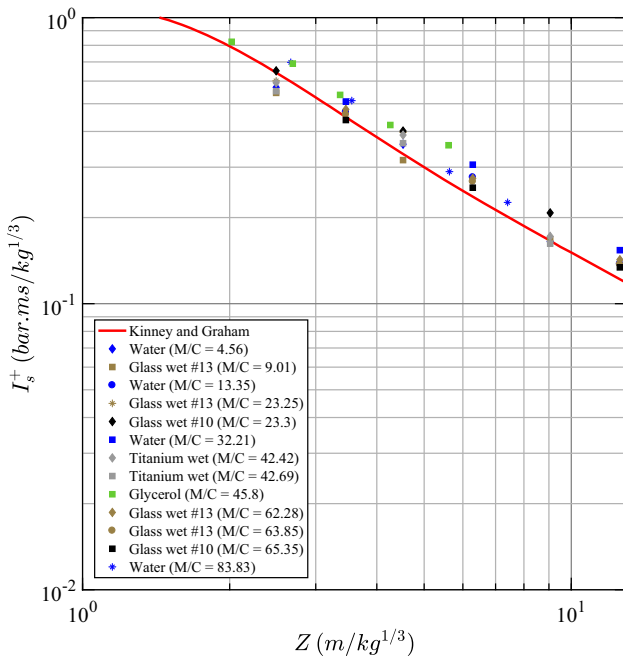
Fig. 29 Scaled positive-phase impulse as a function of scaled distance Z for a high explosive surrounded by a liquid or powder saturated with water

Fig. 30 Scaled impulse as a function of M/C at three different fixed scaled distances Z for liquids or powders saturated with water

Fig. 31 Effective blast wave impulse mitigation as a function of M/C for solid powders and liquids/powders saturated with water in the far field, at three different scaled distances

found to be above the Kinney and Graham curve except for $Z < 3\,\mathrm{m/kg^{1/3}}$. The reproducibility is given by titanium wet with a maximum discrepancy of 6.5% at $Z = 2.49\,\mathrm{m/kg^{1/3}}$. In contrast with powders, liquid mitigants have virtually no influence on the decay of the scaled positive-phase impulse with distance, in comparison with a bare HE charge. Furthermore, from Fig. 30, the scaled impulse does not depend on M/C. No clear trend can be extracted on a material basis except that on average, powders saturated with water appear to have lower impulses than liquids. Also, contrary to solid powders, glass #10 wet has slightly lower impulses compared to glass #13 wet.

Similarly to Fig. 22, Fig. 31 shows the comparison of the average attenuation of the blast positive-phase impulse for solid particles versus liquids (or particles saturated with water) for M/C between 15 and 160, in the far field. Note that the normalized impulse values for liquids/particles saturated with water are higher than unity since impulse values are above the Kinney and Graham curve in Fig. 29. On average, for each type of material, the normalized impulse increases more slowly with scaled distance, though not linearly. For solid powders, a discrepancy between $Z = 6.29\,\mathrm{m/kg^{1/3}}$ and $Z = 12.57\,\mathrm{m/kg^{1/3}}$ is visible for low M/C but disappears at high M/C. At $M/C = 15$, solid powders have impulse values of 72.7, 75.9, 77.6% at, respectively, $Z = 3.46$, 6.29, and $12.57\,\mathrm{m/kg^{1/3}}$, normalized to those for liquids/powders saturated with powders. At $M/C = 160$, the percentages drop to 21.4, 22.9, and 21.8%.
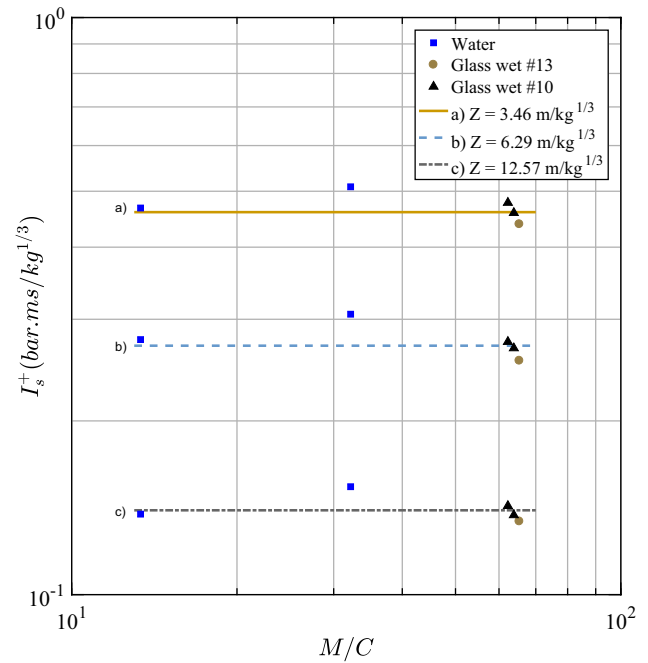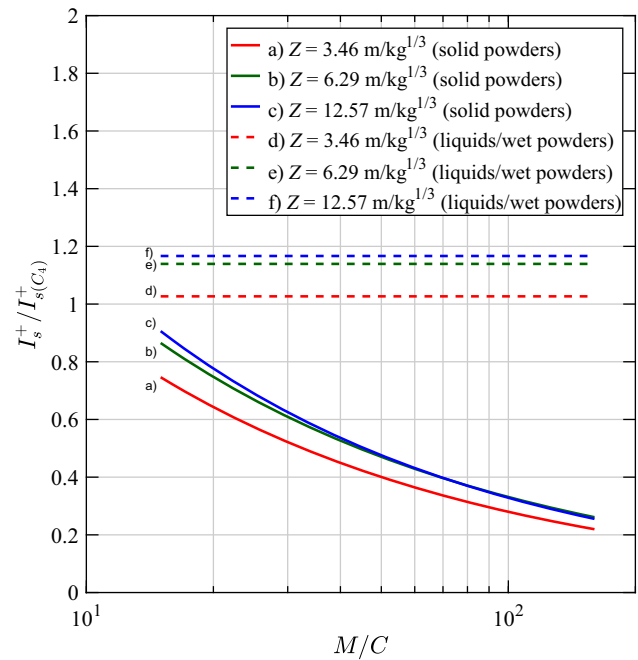
5 Discussion

Figures 12, 13, 17, and 18 demonstrate that the peak blast overpressure from a high-explosive charge may be reduced by more than one order of magnitude by surrounding the

charge with a layer of mitigating material, provided that the mass of mitigant is sufficiently large, relative to the high-explosive mass. The mitigation is most effective in the near field for solid powders, particularly for scaled distances of $Z < 2$ m/kg$^{1/3}$. The attenuation of the peak overpressure is primarily dependent on the M/C ratio, for a given scaled distance as shown in Figs. 14 and 19. Since the mitigant mass, or mass ratio, is the key parameter controlling the effectiveness of blast mitigation, it is likely that the transfer of momentum and heat (investigated numerically in another publication [43]) from the detonation products to the particles is the primary mechanism for reducing the blast overpressure in the near field. Increasing the inert mass surrounding a high-explosive charge will increase the amount of thermal energy extracted from the expanding detonation products. For the case of liquids, which are relatively incompressible, there will be little compaction work done on the liquid as the shock propagates through it, and little evaporation over this short timescale. Hence, the transfer of momentum and heat to the liquid will again be primarily responsible for the mitigation of the peak blast overpressure in the near field.

For the case of solid powders, the compaction of the porous bed and deformation of the particles also contribute to mitigating the blast overpressure. The relative importance of compaction compared with the transfer of heat and momentum can be determined by comparing the average decay of peak blast overpressure as a function of M/C for liquids and solids powders in the near field ($Z = 0.8$ m/kg$^{1/3}$) (see Fig. 22). The absolute value compared to unity for liquids/wet powders (dashed line c) reflects the degree of mitigation due to the heat and momentum transfer, and the difference between this curve and the curve for solid powders (solid line a) is a measure of the additional pressure reduction due to compaction effects. The reduction in pressure due to compaction at low M/C values is less significant than the reduction due to the transfer of heat and momentum, but it is still important. For M/C values above 100, the pressure reduction is dominated by the transfer of heat and momentum and the contribution of compaction is negligible. This result is expected as compaction losses will be most important near the high-explosive charge due to decay of the shock pressure with distance inside the particle bed. With the increase in inert mass around the charge, the compaction losses do not significantly increase, and hence become relatively less important to the overall energy transfer.

In a recent publication, Milne [44] used hydrocode calculations to develop an empirical correlation for the particle velocity obtained during the explosive dispersal and showed that the velocity deficit, in comparison with the conventional Gurney velocity, is largely due to losses during the powder compaction stage. A similar argument likely explains the pressure mitigation effect of powders. Liquids, in contrast with powders, have negligible initial porosity, and hence energy dissipation due to pore collapse does not play a role during shock propagation through the liquid. For powders saturated with water, the interstitial liquid between the particles is capable of supporting stress, and hence preventing the formation of force chains and limiting particle interaction driven by deformation and compaction. Other phenomena play a role during the explosive dispersal of liquids, including cavitation behind the inward-propagating expansion wave generated when the shock wave reaches the liquid surface. Re-compaction of the bubbly liquid generated by cavitation by the expanding explosive products, and breakup of the liquid into droplets and subsequent droplet evaporation will also occur, as discussed in a recent publication on the dynamics of liquid dispersal [25]. It is likely that the energy consumed by these processes is eventually returned to the flow field through particle drag and expansion of the vapor produced, leading to the lack of impulse deficit observed experimentally in the far field.

As a secondary effect, at a specific M/C value, the material properties appear to influence the peak overpressure reduction. In particular, particles that form jets when explosively dispersed show a higher peak overpressure attenuation in the near field compared to particles that are less prone to form jets (i.e., Chronital steel, S-100 steel). A difference of up to 50% in peak overpressure values can be observed (Fig. 15), at given M/C values, between the heavier steel (Chronital steel, the worst mitigant) and the glass powder with the largest particle size (glass #10, the best mitigant). The higher heat capacity of the glass particles [43] and the ability of these particles to deform, crush or fracture more easily is a possible explanation for this difference of mitigation. All materials that are easily deformed, crushed, or fractured (e.g., glass #13, granulated sugar, icing sugar) show mitigation performances closer to the glass #10 powder. Conversely, heavy metal particles, such as S-110 steel, iron, and brass, have peak overpressure values closer to that of Chronital steel. Ductile metals, such as aluminum, as well as hard, but brittle powders like silicon carbide and sand exhibit intermediate values. When homogeneously mixed with silicon carbide, S-110 steel exhibits a higher mitigation performance, suggesting that compaction and fracturing of the brittle component still occurs in a powder mixture. In the case of liquids or powders saturated with water, differences are less with a maximum discrepancy of 20% between water, the best mitigant and glycerol the worst mitigant (Fig. 20). Ethanol and vegetable oil have intermediate peak overpressure values. Factors that may contribute to the difference in the mitigation performances include the heat absorption and the heat required to vaporize the liquids. Indeed, ethanol has a lower latent enthalpy of vaporization on a mass basis [45] and specific heat [46] ($\Delta H_{vap} = 846$ kJ/kg, $c_p = 2.3-2.72$ kJ/(kg K), at temperatures between 0 and 40 °C) compared to water [$\Delta H_{vap} = 2257$ kJ/kg, $c_p = 4.19$ kJ/(kg-K)]. On the other

hand, glycerol is denser than the two previous liquids and possesses a higher heat of vaporization ($\Delta H_{vap} = 974\,kJ/kg$) compared to ethanol but has a slightly higher c_p [$c_p = 2.43\,kJ/(kg\text{-}K)$]. Similar arguments could explain differences in the peak overpressure mitigation in the near field for vegetable oil and sodium polytungstate. Conversely, the addition of particles in liquids (e.g., glycerol with tungsten carbide) or the addition of water to a powder bed may affect the vaporization of the liquids, hence reducing the mitigation performance in the near field. To explore the importance of different liquid properties on blast attenuation more fully, detailed hydrocode calculations are needed, in which the heat transfer to the liquid, liquid fragmentation into droplets and vaporization effects are all considered. Blast attenuation during particle dispersal is explored computationally in a companion paper [47], and while heat transfer effects are considered, liquid fragmentation is not modeled in this work.

The rate of decay of the peak overpressure in the near field ($Z < 2\,m/kg^{1/3}$) for powder and liquid mitigants is less than for an unmitigated high-explosive charge (see Figs. 12, 17). It is likely that the motion of particles influences the blast wave propagation, even if the particle front does not follow closely behind the blast front. It is hypothesized that the particle front is effectively acting as a porous piston, which generates pressure disturbances. Each particle, or group of particles in close proximity, will drive a bow shock ahead of it (if particle velocities are higher than the local speed of sound), which collectively perturb the local flow field. These perturbations are all the more important in the near field where the local particle density is high. These pressure disturbances propagate upstream in the hot, post-shocked air, augmenting the pressure and impulse behind the blast wave. As the blast wave expands radially, it slows down, and ultimately the disturbances are able to catch the blast wave and influence the peak overpressure. In the far field ($Z > 2\,m/kg^{1/3}$), the blast front and front of the cloud of particles are well separated. In this zone, the particle density becomes quite low due to the radial expansion of the particle front, and the particle influence on the blast wave propagation becomes insignificant. Hence, in the far field, the rate of decay of the peak overpressure becomes closer to that of an unmitigated blast wave (Figs. 12, 17) but mitigation performances continue to decrease in the far field (Figs. 16, 21). In the present experiments, combustion in the dispersed material cloud was only observed in a few cases (e.g., for icing sugar and ethanol). However, the combustion was only initiated after the blast propagation and hence had no influence on the blast wave motion.

Jets of solid particles and liquid droplets exhibit somewhat different dynamics. For a given M/C, solid particle jets initially have a lower velocity than liquid jets due to losses during compaction of the particle bed. However, jets of liquid droplets are subject to fragmentation, which increases the droplet surface area and causes the liquid jets to decelerate more rapidly than solid particle jets [25]. Particles accelerate at early times when they are still within the detonation products and hence are not visible by videography. As soon as the particles leave the detonation products, they begin to decelerate due to drag with the surrounding gas and the momentum of the particles will be converted back to momentum of the gas. Hence, even in the far field, pressure disturbances still influence the pressure field behind the blast front and contribute to the blast impulse. Furthermore, all momentum losses by evaporation of the liquid behind the blast front will be converted back into momentum of the gas. As a result, for liquids, the blast momentum is totally recovered behind the leading shock front independently of M/C and the pressure impulse is essentially the same as an unmitigated charge (Fig. 30). For solid powders, a part of the total blast momentum is permanently lost during the compaction and implies a reduction in blast impulse (Fig. 27). By increasing the mass ratio, impulses are reduced similarly to peak overpressures and follow the same decay as a function of M/C (Figs. 28, 31). As noted earlier, the rate of decay is higher at low M/C due to the loss of momentum by compaction but diminishes at high M/C when compaction losses become less significant compared to the transfer of heat and momentum to the particles.

The investigation of the effect of material properties on the peak blast overpressure and positive-phase impulse attenuation is more complex in the far field. Indeed, the blast attenuation in the far field is a consequence of two factors: (i) the energy/momentum loss during the shock propagation in the initial material layer, and (ii) the blast energy/momentum recovery through the motion of the particles mentioned in the previous paragraph. The latter effect depends mainly on the ability of the particles to give their energy back to the flow by drag, which depends on the shape, velocity, size, and density of the dispersed particles. In particular, the largest glass particles (glass #10) attenuate the peak blast overpressure more in the near field than the far field (Fig. 15) but appear to mitigate both the peak overpressure and the impulse less in the far field (Figs. 16, 27). This phenomenon indicates that the blast overpressure recovers faster for the glass #10 particles. This phenomenon is counterintuitive since smaller particles are more subject to drag and should be able to give their energy back to the flow more quickly. Hence, the blast pressure should be higher in the far field for the smallest particles. It is hypothesized that during the compaction of the initial particle bed, the glass #10 particles fracture into smaller fragments than that for the glass #13 powder. In addition, steel particles are found to be better at reducing the blast pressure in the far field, contrary to the near field. This effect can be attributed to the higher particle size of the steel shot, compared to the glass particles (see Table 1), which decreases the overpressure recovery as mentioned earlier. The non-jetting behavior of

the steel particles may also diminish the energy/momentum recovery process compared to jetting powders, although this appears to be a secondary effect since the blast mitigation for steel particles (non-jetting) is on the same order as for iron particles (jetting), which have a similar density. In the case of liquids or solid powders, the comparison between materials in the far field is difficult due to the lack of statistics. Nevertheless, powders saturated with water show, on average, slightly better impulse attenuations than liquids, suggesting that residual compaction can occur during the propagation of the initial shock through wetted powders.

It is found that solid powders are more effective than liquids at mitigating peak blast overpressures and impulses. However, in practical situations, the loading on a structure consists of not only the impulse due to the interaction of the blast wave and subsequent air flow, but also the impulse from the impact of the particles [48]. Hence, in many cases the reduction in blast impulse may be overwhelmed by the particle impulse [49]. Furthermore, to obtain a significant reduction in the peak overpressure in the far field, a large amount of inert material is required relative to the high-explosive mass. For example, to obtain an order of magnitude reduction in blast overpressure at a scaled distance of $Z = 2$ m/kg$^{1/3}$ requires a mass ratio of 50.

6 Conclusions

The mitigation of a blast wave created by the detonation of a high explosive was investigated experimentally. Various types of mitigants including a wide range of solid particles, liquids, and particles saturated with water have been tested. The peak blast wave overpressure was inferred from the analysis of the blast wave motion from the high-speed video records, and the positive-phase blast impulse was determined from side-on pressure transducers at several distances from the charge. The primary results of this study are as follows:

1. Solid powders, liquids, or powders saturated with a liquid can be used as blast wave mitigants. However, solid powders outperform liquids with respect to mitigating the blast wave peak overpressure, especially in the near field and at low ratios of the mass of mitigant to the high-explosive charge. The difference in mitigation performance is likely due to the energy loss during the compaction and deformation of solid powders at early times.
2. The comparison between mitigation efficiencies of solid powders and liquids suggests that mitigation is mainly due to the transfer of heat and momentum. However, at low M/C, shock-induced compaction of the particle bed and particle deformation of the particles is a significant contributing factor for the blast mitigation for solid

powders. At high M/C, the relative contribution of deformation/compaction compared to the transfer of heat and momentum becomes negligible.
3. The decay of the blast peak overpressure for both granular solid and liquid mitigants as a function of M/C follows a weak power law function. The decay of blast impulse as a function of M/C for the solid powders also exhibits a power law decay. However, in the case of the liquids or liquid-saturated powders, blast impulses in the far field are essentially the same or slightly higher as that of an unmitigated charge with the same high-explosive mass and does not depend on the mass ratio.
4. The degree of blast mitigation in the near field with either powders or liquids/wet powders surrounding a charge is primarily dependent on M/C. The material properties play a secondary role in the mitigation process. In the case of solid particles, jetting powders (all the powders tested except steel) show higher mitigation performances than non-jetting powders (steel), by up to 50%. Glass particles show the best peak blast overpressure and impulse attenuation. Factors that likely contribute to the good performance of glass particles include its high heat capacity, and the tendency of the powder to deform and fracture. Other easily crushable, brittle, or ductile powders (e.g., sugar, silicon carbide, sand, aluminum) are found to attenuate the blast more than dense metallic powders (iron, brass, S-110 steel, and Chronital steel). In the case of liquids, the difference in mitigation performance is small (up to 20%). Water appears to attenuate the blast the most in the near field possibly due to its higher heat capacity and heat of vaporization. Water-saturated powders attenuate the blast slightly more in the far field compared to liquids, indicating that residual compaction may occur during the propagation of the shock through the initial bed.
5. It is hypothesized that the slower rate of decay of the peak blast overpressure in the near field for a mitigated charge versus an equivalent bare charge is due to pressure support induced by the motion of the mitigant which effectively acts as a porous piston. The local pressure disturbances from the particle–flow interaction eventually catch up to the leading shock front and perturb the peak overpressure. This particle–blast interaction, which depends principally on the properties of the dispersed materials (e.g., shape, particle/droplet size, density), generates a complex blast mitigation dependence on material properties in the far field. In a companion paper, the details of the particle–blast wave interaction are explored more fully with hydrocode calculations [47].

In future work, a more precise quantification of the influence of material properties on the blast attenuation could be achieved by improving the accuracy of the videography

method. The inclusion of a uniform background behind the charge and increasing the spatial resolution of the high-speed videography could significantly improve the analysis. Also, the use of small mass of mitigant to charge ratio would highlight the discrepancy. The assessment of damage to nearby structures due to the combined blast-particle impulse is a natural extension of the present work. Finally, the effect of particles embedded within a high explosive, in comparison with stratified explosive-particle systems, is of interest.

References

1. Cheng, M., Hung, K.C., Chong, O.Y.: Numerical study of water mitigation effects on blast wave. Shock Waves **14**(3), 217–223 (2005). doi:10.1007/s00193-005-0267-4

2. Allen, R.M., Kirkpatrick, D.J., Longbottom, A.W., Milne, A.M., Bourne, N.K.: Experimental and numerical study of free-field blast mitigation. AIP Conf. Proc. **706**, 823–826 (2004). doi:10.1063/1.1780363

3. Resnyansky, A.D., Delaney, T.G.: Experimental study of blast mitigation in a water mist. Technical Report, DSTO Defence Science and Technology Organisation, Edinburgh, South Australia, Australia (2006)

4. Schwer, D., Kailasanath, K.: Blast mitigation by water mist (3)—mitigation of confined and unconfined blasts. Technical Report NRL/MR/6410-06-8976, Naval Research Laboratory, Washington, DC, USA (2006)

5. Del Prete, E., Chinnayya, A., Domergue, L., Hadjadj, A., Haas, J.-F.: Blast wave mitigation by dry aqueous foams. Shock Waves **23**(1), 39–53 (2013). doi:10.1007/s00193-012-0400-0

6. Gelfand, B.E.: Blast waves attenuation in two-phase media. In: Symposium on Interdisciplinary Shock Wave Research, pp. 150–166, Sendai, Japan (2004)

7. Raspet, R., Powers, J.M., Panczak, T.D., Butler, P.B., Jahani, F.: Attenuation of blast waves using foam and other materials. Technical Report N-89/01, US Army Construction Engineering Construction Laboratory, Champaign, IL, USA (1989)

8. Kitagawa, K., Yamashita, S., Takayama, K., Yasuhara, M.: Attenuation properties of blast wave through porous layer. In: Hannemann, K., Seiler, F. (eds.) Shock Waves, pp. 73–78. Springer, Berlin, Heidelberg (2009). doi:10.1007/978-3-540-85168-4_10

9. Hartman, W.F., Boughton, B.A., Larsen, M.E.: Blast mitigation capabilities of aqueous foam. Technical Report SAND2006-0533, Sandia National Laboratories, Albuquerque, NM, USA (2006). doi:10.2172/877732

10. Britan, A., Shapiro, H., Ben-Dor, G.: Foams for blast mitigation. In: Stevenson, P. (ed.) Foam Engineering: Fundamentals and Applications, chap. 19, pp. 477–512. Wiley, Hoboken (2012)

11. Nesterenko, V.F.: Shock (blast) mitigation by soft condensed matter. In: MRS Symp. Proc., vol. 759, pp. MM4.3.1–4.3.12 (2003). doi:10.1557/PROC-759-MM4.3

12. Britan, A., Ben-Dor, G., Igra, O., Shapiro, H.: Shock waves attenuation by granular filters. Int. J. Multiph. Flow **27**(4), 617–634 (2001). doi:10.1016/S0301-9322(00)00048-3

13. Medvedev, S.P., Frolov, S.M., Gel'fand, B.E.: Attenuation of shock waves by screens of granular material. J. Eng. Phys. **58**(6), 714–718 (1990). doi:10.1007/BF00872723

14. Langhorst, B., Cook, C., Schondel, J., Chu, H.S.: Material systems for blast-energy dissipation. In: IMPLAST 2010 Conference, pp. 1–8. Society for Experimental Mechanics, Providence, RI, USA (2010)

15. Endo, K., Kitagawa, K., Yasuhara, M.: Diffusion effect of blast pressure in porous complex media. In: 39th AIAA Fluid Dynamics Conference, Number June in Fluid Dynamics and Co-located Conferences, San Antonio, Texas, AIAA Paper 2009-3569. American Institute of Aeronautics and Astronautics (2009). doi:10.2514/6.2009-3569

16. Wang, Z., Lu, Y.: Numerical analysis on dynamic deformation mechanism of soils under blast loading. Soil Dyn. Earthq. Eng. **23**(8), 705–714 (2003). doi:10.1016/S0267-7261(03)00076-9

17. Lu, Y., Wang, Z., Chong, K.: A comparative study of buried structure in soil subjected to blast load using 2D and 3D numerical simulations. Soil Dyn. Earthq. Eng. **25**(4), 275–288 (2005). doi:10.1016/j.soildyn.2005.02.007

18. Ambrosini, R.D., Luccioni, B.M., Danesi, R.F., Riera, J.D., Rocha, M.M.: Size of craters produced by explosive charges on or above the ground surface. Shock Waves **12**(1), 69–78 (2002). doi:10.1007/s00193-002-0136-3

19. Loiseau, J., Pontalier, Q., Milne, A., Goroshin, S., Frost, D.L.: Terminal velocity of liquids and granular materials accelerated by a high explosive. In: 24th International Symposium on Military Aspects of Blast and Shock (MABS 24), pp. 1–13, Halifax, Canada (2016)

20. Gurney, R.W.: The initial velocities of fragments from bombs, shells, and grenades. Technical Report (405), BRL, Aberdeen Proving Ground, MD, USA (1943)

21. Cooper, P.W.: Explosives Engineering. Wiley-VCH, Weinheim (1996)

22. Frost, D.L., Loiseau, J., Marr, B.J., Goroshin, S., Gregoire, Y., Petel, O., Goroshin, S., Zhang, F.: Particle segregation during explosive dispersal of binary particle mixtures. Phys. Fluids **24**(9), 1–6 (2012). doi:10.1063/1.4751876

23. Frost, D.L., Grégoire, Y., Petel, O., Goroshin, S., Zhang, F.: Particle jet formation during explosive dispersal of solid particles. Phys. Fluids **24**, 091109 (2012). doi:10.1063/1.4751876

24. Milne, A.M., Floyd, E., Longbottom, A.W., Taylor, P.: Dynamic fragmentation of powders in spherical geometry. Shock Waves **24**(5), 501–513 (2014). doi:10.1007/s00193-014-0511-x

25. Milne, A.M., Longbottom, A., Frost, D.L., Loiseau, J., Goroshin, S., Petel, O.: Explosive fragmentation of liquids in spherical geometry. Shock Waves **27**, 383–393 (2017). doi:10.1007/s00193-016-0671-y

26. Loiseau, J., Pontalier, Q., Milne, A.M., Goroshin, S., Frost, D.L.: Terminal velocity of liquids and granular materials dispersed by a high explosive. Shock Waves **28**(3) (2018). doi:10.1007/s00193-018-0822-4

27. Kleine, H., Timofeev, E., Takayama, K.: Laboratory-scale blast wave phenomena—optical diagnostics and applications. Shock Waves **14**(5–6), 343–357 (2005). doi:10.1007/s00193-005-0279-0

28. Panigrahi, P.K., Muralidhar, K.: Laser schlieren and shadowgraph. In: Methods in Heat and Mass Transfer: Visualization and Analysis, chap. 2, pp. 23–46. Springer, New York (2012). doi:10.1007/978-1-4614-4535-7_2

29. Venkatakrishnan, L., Meier, G.E.A.: Density measurements using the background oriented schlieren technique. Exp. Fluids **37**(2), 237–247 (2004). doi:10.1007/s00348-004-0807-1

30. Ramanah, D., Raghunath, S., Mee, D.J., Rösgen, T., Jacobs, P.A.: Background oriented schlieren for flow visualisation in hypersonic impulse facilities. Shock Waves **17**(1–2), 65–70 (2007). doi:10.1007/s00193-007-0097-7

31. Hargather, M.J.: Background-oriented schlieren diagnostics for large-scale explosive testing. Shock Waves **23**(5), 529–536 (2013). doi:10.1007/s00193-013-0446-7

32. Sommersel, O.K., Bjerketvedt, D., Christensen, S.O., Krest, O., Vaagsaether, K.: Application of background oriented schlieren for quantitative measurements of shock waves from explosions. Shock Waves **18**(4), 291–297 (2008). doi:10.1007/s00193-008-0142-1

33. Yamamoto, S., Tagawa, Y., Kameda, M.: Application of background-oriented schlieren (BOS) technique to a laser-induced underwater shock wave. Exp. Fluids **56**, 93 (2015). doi:10.1007/s00348-015-1960-4

34. Anderson, J.G., Parry, S.L., Ritzel, D.V.: Time dependent blast wave properties from shock wave tracking with high speed video. In: 24th International Symposium on Military Aspects of Blast and Shock (MABS 24), pp. 1–20, Halifax, Canada (2016)

35. Campbell, I.J., Pitcher, A.S.: Shock waves in a liquid containing gas bubbles. Proc. R. Soc. Lond. A **243**(1235), 534–545 (1958). doi:10.1098/rspa.1958.0018

36. Dewey, J.M.: The properties of a blast wave obtained from an analysis of the particle trajectories. Proc. R. Soc. Lond. A **324**, 275–299 (1971). doi:10.1098/rspa.1971.0140

37. Kleine, H., Dewey, J.M., Ohashi, K., Mizukaki, T., Takayama, K.: Studies of the TNT equivalence of silver azide charges. Shock Waves **13**(2), 123–138 (2003). doi:10.1007/s00193-003-0204-3

38. Kinney, G.F., Graham, K.J.: Explosive Shocks in Air, 2nd edn. Springer, New York (1985). doi:10.1007/978-3-642-86682-1

39. Swisdak, M.M. Jr.: Explosion effects and properties—part 1—explosion effects in air. Technical Report NSWC/WOL/TR-75-116, White Oak, Silver Spring, Maryland (1975)

40. Bogosian, D., Yokota, M., Rigby, S.: TNT equivalence of C-4 and PE4: a review of traditional sources and recent data. In: 24th International Symposium on Military Aspects of Blast and Shock (MABS 24), pp. 1–15 (2016)

41. Brode, H.L.: Blast wave from a spherical charge. Phys. Fluids **2**(2), 217–229 (1959). doi:10.1063/1.1705911

42. Biss, M.M., McNesby, K.L.: Optically measured explosive impulse. Exp. Fluids **55**(6), 1749 (2014). doi:10.1007/s00348-014-1749-x

43. Pontalier, Q., Lhoumeau, M., Frost, D.L.: Blast wave mitigation in granular materials. In: 20th Biennial APS Conference on Shock Compression of Condensed Matter (SCCM), pp. 1–5, St. Louis, MO, USA. AIP Conference Proceedings (2017)

44. Milne, A.M.: Gurney analysis of porous shell. Propellants Explos. Pyrotech. **41**(4), 665–671 (2016). doi:10.1002/prep.201600016

45. https://www.engineeringtoolbox.com/fluids-evaporation-latent-heat-d_147.html

46. https://www.engineeringtoolbox.com/specific-heat-fluids-d_151.html

47. Pontalier, Q., Lhoumeau, M.G., Milne, A.M., Longbottom, A.W., Frost, D.L.: Numerical investigation of particle–blast interaction during explosive dispersal of liquids and granular materials. Shock Waves **28**(3) (2018). doi:10.1007/s00193-018-0820-6

48. Cheesman, R., Tilbury, C.: Blast and debris in the near field—diagnostic techniques and calculational tools to predict combined impulse loading. In: 24th International Symposium on Military Aspects of Blast and Shock (MABS 24), pp. 1–20, Halifax, Canada (2016)

49. Frost, D.L., Ornthanalai, C., Zarei, Z., Tanguay, V., Zhang, F.: Particle momentum effects from the detonation of heterogeneous explosives. J. Appl. Phys. **101**(11), 113529 (2007). doi:10.1063/1.2743912